Pervasive silicification and hanging wall overplating along the 13°20'N oceanic detachment fault (Mid-Atlantic Ridge)

D. Bonnemains, J. Escartin, C. Mével, M. Andreani, Anne Verlaguet

AGU PUBLICATIONS

Geochemistry, Geophysics, Geosystems

RESEARCH ARTICLE
10.1002/2017GC006846

Pervasive silicification and hanging wall overplating along the 13°20′N oceanic detachment fault (Mid-Atlantic Ridge)

D. Bonnemains[1], J. Escartín[1], C. Mével[1], M. Andreani[2], and A. Verlaguet[3]

[1]Institut de Physique du Globe de Paris, CNRS UMR 7154, Paris, France, [2]Laboratoire de Géologie de Lyon, UMR 5672, ENS, Université Lyon 1, Lyon, France, [3]Institut des Sciences de la Terre de Paris, CNRS, Sorbonne Universités, Université Paris 6, Paris, France

Key Points:
- 13°20′N detachment fault zone exposed at seafloor is composed of mafic material overplated from the hanging wall during extension
- Overplating likely initiates at the base of the dyke complex associated with the magmatic crust from the hanging wall
- Detachment fault deformation coeval with hydrothermal fluid flow and associated quartz mineralization under greenschist conditions

Supporting Information:
- Supporting Information S1
- Table S1

Correspondence to:
D. Bonnemains,
diane.bonnemains@gmail.com

Citation:
Bonnemains, D., J. Escartín, C. Mével, M. Andreani, and A. Verlaguet (2017), Pervasive silicification and hanging wall overplating along the 13°20′N oceanic detachment fault (Mid-Atlantic Ridge), *Geochem. Geophys. Geosyst.*, *18*, 2028–2053, doi:10.1002/2017GC006846.

Received 30 JAN 2017
Accepted 5 MAY 2017
Accepted article online 22 MAY 2017
Published online 8 JUN 2017

Abstract The corrugated detachment fault zone of the active 13°20′N oceanic core complex (Mid-Atlantic Ridge) was investigated with a deep-sea vehicle to assess the links between deformation, alteration, and magmatism at detachment fault zones. We present a study of 18 in situ fault rock samples from striated fault outcrops on the flanks of microbathymetric corrugations. All the samples are mafic breccias that are mostly derived from a diabase protolith, with two of them also showing mixing with ultramafic clasts. Breccias are cataclastic and display variable deformation textures, recording numerous slip events, and showing pervasive silicification throughout the fault zone. Deformation-silicification relationships are also complex, showing both static and syntectonic quartz precipitation; undeformed quartz overprints the fault breccia textures, and reflective and striated fault surfaces cross-cut silicified rocks. In situ detachment fault rocks are mainly fault breccias with almost exclusively basaltic clasts, with rare ultramafic ones, a lithology and texture never observed previously at other oceanic detachment fault zones. We propose the lower dyke complex in the hanging wall crust at the volcanic rift valley floor is the most plausible diabase source. Mechanical mixing of predominantly mafic and rare ultramafic clasts suggests an underlying ultramafic footwall and that mafic accretion operates in the shallowest crust (1–2 km), at the base of the dyke complex at temperatures >400°C. Silicification is produced by silica-rich fluids syntectonically channeled along the fault zone, and likely derived from hydrothermal alteration of basaltic rocks, likely mixed with serpentinization-derived fluids.

Plain Language Summary This paper presents a textural, mineralogical, and microstructural study of the fault rocks recovered in situ on the 13°20′N detachment fault zone (Mid-Atlantic ridge) during the ODEMAR cruise in 2013. This detachment is unique for the presence of mafic material integrated within the fault zone as breccias and the pervasive silicification observed throughout all the detachment surface. Our paper discusses the origin of the mafic breccias and proposes that they were captured from the base of the dyke complex within the hanging wall during the fault exhumation. Our study reveals furthermore that quartz mineralization occurred in depth during the exhumation and is likely linked with the presence of mafic material within the fault zone. Our study indicates a complex relationship between silicification and deformation during which quartz (re)crystallized under quasi-static conditions between periods of deformation. This work also demonstrates that extreme strain localization can be achieved in the absence of weak alteration phases (talc, serpentine) but with instead high-friction material (quartz), suggesting that elevated pore fluid pressures play an important role.

1. Introduction

Along slow and ultraslow spreading ridges, tectonic processes play a major role accommodating seafloor spreading in combination with magmatism. With low magma budgets on-axis, deformation can localize along long-lived faults exhuming lower crust and upper mantle materials at the seafloor, leading to the formation of oceanic core complexes (OCCs) [e.g., *Buck et al.*, 2005; *Tucholke et al.*, 2008; *Olive et al.*, 2010]. OCCs are often characterized by broad domes that rise above surrounding seafloor and display spreading-parallel corrugations along the exposed fault surface [*Cann et al.*, 1997; *Blackman et al.*, 1998; *Tucholke et al.*, 1998; *Smith et al.*, 2006]. Numerous corrugated OCCs have been identified to date, mainly along the Mid-Atlantic Ridge (MAR) and the Southwest Indian Ridge, both at inside corner highs and away from transform

faults [*Cann et al*., 1997; *Blackman et al*., 1998; *Dick et al*., 2000; *MacLeod et al*., 2002; *Escartín et al*., 2003; *Smith et al*., 2006, 2008]. It has been estimated that spreading is associated with detachment faulting along ~50% of the northern MAR [*Escartín et al*., 2008], and the ubiquity of detachments confirms that these structures represent an important end-member mode of seafloor spreading [*Escartín et al*., 2008; *Cannat et al*., 2009; *Escartín and Canales*, 2010]. Detachment faulting appears to be linked to both seismicity [*Escartín et al*., 2008; *Simao et al*., 2010] and hydrothermal activity [*Escartín et al*., 2008; *McCaig et al*., 2010; *Fouquet et al*., 2010]. There is also geological evidence of fluid flow and syntectonic fluid-rock interaction along the fault zone [*Escartín et al*., 2003; *Boschi et al*., 2006; *Karson et al*., 2006; *McCaig et al*., 2007]. The microseismicity observed to depths of ~7 km along the TAG detachment fault [*deMartin et al*., 2007] provides a fault-controlled mechanism for deep fluid penetration near-axis where heat could drive long-term, high-temperature hydrothermal convection. A consequence of the interaction between fluids and mantle rocks is the formation of weak hydrous minerals such as talc and serpentine, assumed to promote strain localization along these fault planes [e.g., *Escartín et al*., 2001; *Schroeder and John*, 2004].

Some of the numerous OCCs identified during shipboard bathymetric surveys have been extensively studied and sampled, providing the geological data critical to understand the deformation mechanisms operating within the fault zone. Dredging, drilling, and studies involving deep-sea vehicles have been carried out on several core complexes along the MAR, including Atlantis Massif (30°N) [*Schroeder and John*, 2004; *Blackman et al*., 2006; *Boschi et al*., 2006; *Karson et al*., 2006], 15°45′N [*MacLeod et al*., 2002; *Escartín et al*., 2003; *Schroeder et al*., 2007] and Kane (23°N) [*Dick et al*., 2008; *Hansen et al*., 2013]; along the Southwest Indian Ridge at Atlantis Bank [*Dick et al*., 2000; *Miranda and John*, 2010] and FUJI dome [*Searle et al*., 2003]; and along the Mid-Cayman Rise [*Hayman et al*., 2011]. These studies show that the fault zone is complex and compositionally heterogeneous with both gabbros and peridotites in varying abundances, and more or less recrystallized. These studies also report the presence of minor mafic material (primarily dyke injections). In terms of deformation mechanisms, both ductile and brittle deformation textures may be observed along the fault zone. There is also evidence for local high-temperature plastic deformation along high-temperature mylonitic shear zones in gabbroic rocks recovered from OCCs that display abundant lower crustal rocks, e.g., at Kane [*Dick et al*., 2008; *Hansen et al*., 2013], Atlantis Bank [*Cannat et al*., 1991; *Dick et al*., 2000], and Mid-Cayman Rise [*Hayman et al*., 2011]. However, their direct relationship with the detachment fault remains unclear, and this plastic deformation may be acquired prior to the incorporation of these materials into the detachment fault zone (e.g., deformation related to magma emplacement in the lithosphere). Lower-temperature ductile deformation characterizes detachments where ultramafic rocks predominate and results in the formation of talc-chlorite schists and amphibolites, e.g., at Atlantis Massif [*Schroeder et al*., 2004], and 15°45′N [*Escartín et al*., 2003], and other detachments along the MAR [*Picazo et al*., 2012]. Both brittle and semibrittle deformation are observed in all detachments, in some cases showing overprinting of the previous deformation features during the cooling evolution of the system, as shown in the studies listed above.

To understand deformation mechanisms, composition, and fluid-rock-deformation interactions along an oceanic detachment fault zone, we investigate the detachment fault zone at 13°20′N along the MAR. Previous studies here have used surface bathymetry, deep-towed side-scan sonar imaging, dredging, and seabed drilling [*MacLeod et al*., 2009; *Mallows and Searle*, 2012], showing that this detachment is well developed structurally and likely active, since it roots at the ridge axis and its corrugated surface is not disrupted by late faulting. These characteristics make it an ideal site to study processes associated with detachment fault formation and evolution. This has led to new investigations using an Autonomous Underwater Vehicle (AUV) for microbathymetric mapping, and a remotely operated vehicle (ROV) for observation and sampling [*Escartín et al*., 2017]. In this study, we present field geological observations and analyses of fault rocks recovered from the corrugated fault zone with the deep-sea ROV VICTOR (IFREMER, France). We focus our study on 18 fault rocks sampled from 7 fault outcrops along the corrugated detachment surface, which are unequivocally in situ. We present results on their composition and microstructures to constrain deformation mechanisms and fluid-rock interactions. These observations allow us to propose a model for the evolution and behavior of the fault during its exhumation, and the links to fluid flow.

2. Geological Setting

The oceanic crust formed at the MAR between the Fifteen Twenty and the Marathon transform faults displays contrasting morphologies along axis [*Escartín and Cannat*, 1999; *Smith et al*., 2006, 2008]. The ridge

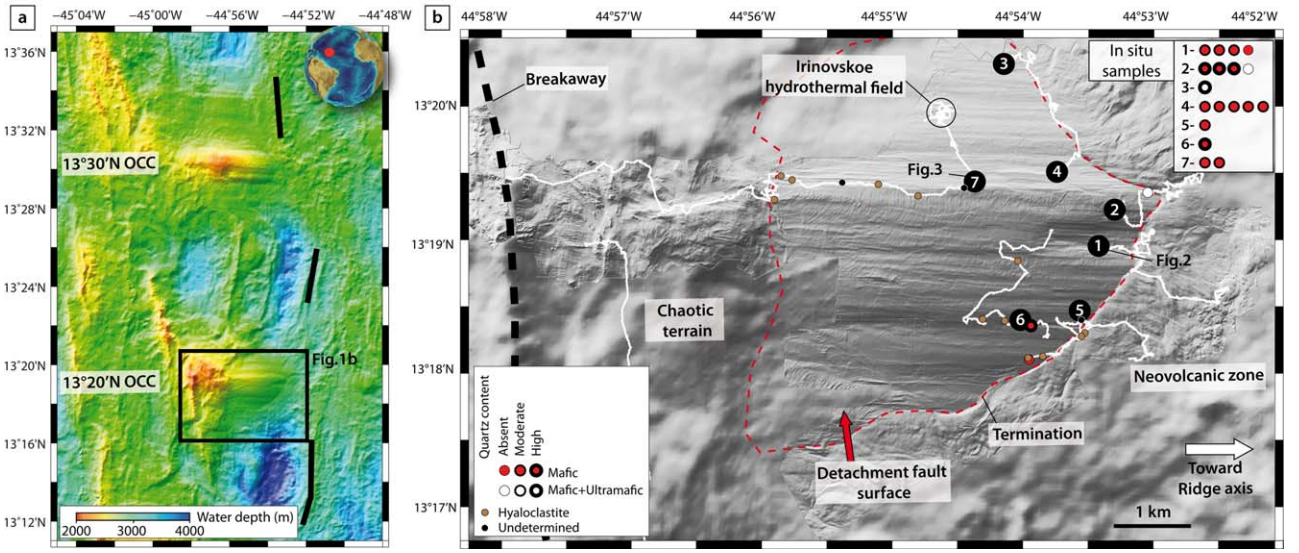

Figure 1. (a) Multibeam shipboard bathymetry data of the 13°20′N detachment region, showing the 13°20′N core complex (black box) that is likely active [*MacLeod et al*., 2009; *Escartín et al*., 2017], adjacent to the ridge axis (black lines). (b) Shaded relief microbathymetry acquired with the AUV Abyss (GEOMAR), collected during the ODEMAR cruise at 13°20′N OCC, complemented with shipboard bathymetry. White lines correspond to the tracks of 10 ROV VICTOR dives. Fault surface outcrops that have been identified and sampled with the ROV are shown by black circles with a number (reported in Table 1) for the in situ samples. Characteristics and degree of silicification of in situ samples are specified in the inset with their corresponding outcrop number. Ex situ samples described in the text and listed in Table 2 are also positioned along ROV tracks.

around 14°N is symmetrical, with abyssal hills parallel to the ridge axis, and can be interpreted as magmatically robust. By contrast, the areas to the North and to the South show numerous large-offset faults and irregular massifs that correspond to OCCs, which often show corrugated detachment fault surfaces. These detachment-dominated corridors show a thin crust attributed to low magma supply relative to the more magmatic 14°N area [*Smith et al*., 2008; *Mallows and Searle*, 2012]. Here the oceanic lithosphere is associated with significant extension and tectonic rotation along these large fault scarps [*MacLeod et al*., 2009; *Schouten et al*., 2010], in addition to several active hydrothermal fields, such as Logachev, Ashadze, or Semyenov, among others [*Beltenev et al*., 2003, 2007; *Fouquet et al*., 2008; *Escartín et al*., 2017].

This study targets the 13°20′N OCC, located along the MAR's Western rift valley wall, and that roots at the rift valley floor in the immediate vicinity of the ridge axis (Figure 1a). This OCC exhibits a domal structure ∼5 km wide along axis that rises ∼1 km above the nearby axial valley. The detailed morphology of this detachment demonstrates that it is well preserved and unfaulted (Figure 1b) [*Escartín et al*., 2017]. This OCC has been extensively studied in recent years with near-bottom, high-resolution sonar mapping [*MacLeod et al*., 2009; *Mallows and Searle*, 2012], in addition to camera tows and sampling [*Cherkashev et al*., 2013]. In 2013, we conducted the ODEMAR cruise to collect near-bottom multibeam bathymetry, imagery, and samples, and main geological observations and detachment-related processes are detailed elsewhere [*Escartín et al*., 2017]. The detachment fault plane is exposed at the seafloor as it emerges from the rift valley floor at an angle of ∼15° along the hanging wall cutoff (termination). The fault flattens progressively at ∼3 km off axis, where it summits ∼900 m above the hanging wall cutoff. The microbathymetric corrugations, parallel to the spreading direction, have amplitudes of <20 m extending up to 2 km along-extension [*Escartín et al*., 2017]. Further off-axis, between the corrugated surface and the detachment breakaway ridge (footwall cutoff, Figure 1b), the seafloor relief is elevated and rougher, corresponding to the chaotic terrain as described for this OCC [*Escartín et al*., 2017]. This area yields abundant basalt and dyke rock samples and is interpreted as a high-angle fault scarp that has undergone mass wasting, rotation, and rafting off-axis, leading to the emergence of the striated fault at the seafloor. Hydrothermal activity at this OCC is restricted to the active Irinovskoe hydrothermal field on the north facing slope of the corrugated surface (Figure 1b), where several black smokers vent at temperatures of up to 360°C [*Escartín et al*., 2017]. Previous dredging conducted on the 13°20′N OCC recovered lithology consistent with the exhumation of deep lithospheric levels [*MacLeod et al*., 2009]. A detailed description of the different tectonic and structural features of this OCC, and the lithologies recovered, is provided elsewhere [*Escartín et al*., 2017].

AGU Geochemistry, Geophysics, Geosystems

10.1002/2017GC006846

Table 1. Summary of Fault Rocks Recovered Both In Situ and Sub–In Situ at the Seven Fault Outcrops of the 13°20′N Corrugated Detachment Surface[a]

				Latitude N		Longitude W											
Outcrop #	Outcrop Length × Width (Distance[b])	Sample # ODM_ROC_	Referred to As	(°)	(min)	(°)	(min)	Depth (m)	In Situ	Rock Type	Texture	Sample Surface and Striations[d]	Slip Zone	Clast Alteration[e]	Protolith	Quartz Content	Sulfides[f]
1	25 m × 3–6 m	V547_114	ODM114	13	18.956	−44	53.429	3158	Yes[c]	Mafic	Clast-supported breccia	–s (1), E-W	Two slip zones	Pl, Amp, Chl	Mafic	Moderate	
(see Figure 2)	(∼400 m)	V547_115	ODM115	13	18.956	−44	53.426	3159	Yes	Mafic	Clast of breccia		Absent	Px, Pl, Amp, Chl	Pillow	Absent	
		V547_117	ODM117	13	18.957	−44	53.428	3158	Sub	Mafic	Clast-supported breccia		Absent	Pl, Amp, Chl	Mafic	Moderate	
		V547_119	ODM119	13	18.956	−44	53.431	3155	Yes[c]	Mafic	Clast-supported breccia	–s (1), E-W	Absent	Pl, Chl	Mafic	Moderate	
2	80 m × 6 m	V552_215	ODM215	13	19.218	−44	53.306	3114	Yes[c]	Mafic	Matrix-supported breccia	–s (2), –m (2), E-W	Four slip zones	Chl, Qz	Diabase	High	
(see supporting information Figure S1)	(∼600 m)	V552_216	ODM216	13	19.217	−44	53.308	3114	Yes[c]	Mafic	Matrix-supported breccia	–s (2), –m (1), E-W	Two slip zone	Chl, Qz	Diabase	High	
		V552_217	ODM217	13	19.217	−44	53.309	3113	Yes[c]	Mafic/ ultramafic	Matrix-supported breccia	–s (1), –m (1), E-W	Four slip zones	Tc, Chl	Mafic + ultramafic	Absent	
		V552_218	ODM218	13	19.216	−44	53.276	3133	Yes[c]	Mafic	Matrix-supported breccia	–s (1), –m (1), E-W	Six slip zones	Chl, Qz	Diabase	High	Pyr + Cpy + Pyrr
3 (see supporting information Figure S2)	>10 m × <1 m (∼200 m)	V551_173	ODM173	13	20.395	−44	54.031	3218	Yes	Mafic/ ultramafic	Matrix-supported breccia		Absent	Tc, Chl	Mafic + ultramafic	High	Pyr + Cpy
4	>10 m × 5 m	V551_192	ODM192	13	19.511	−44	53.742	2927	Sub	Mafic	Clast-supported breccia		Absent	Pl, Amp, Chl	Diabase	Moderate	
(see supporting information Figure S3)	(∼600 m)	V551_193	ODM193	13	19.510	−44	53.744	2924	Yes	Mafic	Clast-supported breccia	–s (1), E-W	Two slip zones	Pl, Amp, Chl	Diabase	Moderate	
		V551_194	ODM194	13	19.514	−44	53.749	2922	Yes	Mafic	Clast-supported breccia		Absent	Pl, Amp, Chl	Diabase	Moderate	
		V551_195	ODM195	13	19.512	−44	53.748	2922	Sub	Mafic	Clast-supported breccia		Absent	Pl, Amp, Chl	Diabase	Moderate	
		V551_196	ODM196	13	19.512	−44	53.750	2925	Sub	Mafic	Clast-supported breccia		Absent	Pl, Amp, Chl	Diabase	Moderate	
5 (see supporting information Figure S4)	>20 m × 2 m (∼100 m)	V549_128	ODM128	13	18.396	−44	53.539	3310	Yes	Mafic	Clast-supported breccia + late foliation	–s (2), –m (2), E-W	Absent	Px, Pl, Amp, Chl	Mafic	Moderate	
6 (see supporting information Figure S5)	>20 m × 1 m (∼800 m)	V550_155	ODM155	13	18.399	−44	54.039	3104	Yes[c]	Mafic	Matrix-supported breccia	–s (1), –m (1), E-W	Five slip zones	Chl, Qz	Diabase	High	Pyr
7	90 m × 5 m	V553_224	ODM224	13	19.426	−44	54.355	2633	Yes[c]	Mafic	Clast-supported breccia + late foliation	–s (2), –m (2), E-W	Absent	Px, Pl, Amp, Chl	Mafic	Moderate	
(see supporting information Figure 3)	(∼2.400 m)	V553_226	ODM226	13	19.420	−44	54.391	2620	Yes[c]	Mafic	Clast-supported breccia	–s (1), –m (1), E-W	Two slip zones	Px, Pl, Chl	Mafic	Moderate	

[a]The outcrop number corresponds to those in Figure 1b, with the corresponding figure calls for each outcrop.
[b]Distance from hanging wall cutoff.
[c]Oriented samples.
[d]Surface characteristics: –s, striated surface; –m, mirror aspect; (N) observed on N faces; E-W, orientation of striations.
[e]Mineral abreviations: Amph, amphibole; Chl, chloritre; Qz, quartz; Pl, plagioclase; Px, pyroxene; Tc, Talc.
[f]Mineral abreviations: Cpy, chalcopyrite; Pyr, pyrite; Pyrr, pyrrhotite.

Table 2. Characteristics of Ex Situ, Deformed Samples Collected on the 13°20′N MAR Corrugated Detachment Surface (See Figure 1b)[a]

		Latitude N		Longitude W				
Sample # ROV_rock_	Referred to As	(°)	(min)	(°)	(min)	Depth (m)	Description	Deformation Origin
V549_129[b]	ODM129	13	18.393	−44	53.524	3315	Mafic breccia	Undetermined
V549_137	ODM137	13	18.326	−44	53.560	3331	Metapillow breccia	Hyaloclastite
V549_139[b]	ODM139	13	18.362	−44	53.562	3312	Metapillow breccia	Hyaloclastite
V549_149	ODM149	13	18.134	−44	53.852	3316	Metapillow breccia	Hyaloclastite
V549_150[b]	ODM150	13	18.116	−44	53.961	3290	Talc schist	Fault related
V549_151[b]	ODM151	13	18.110	−44	53.956	3294	Metapillow breccia	Hyaloclastite
V550_153[b]	ODM153	13	18.363	−44	53.942	3158	Mafic breccia	Fault related
V550_157	ODM157	13	18.400	−44	54.144	3066	Metapillow breccia	Hyaloclastite
V550_159[b]	ODM159	13	18.410	−44	54.312	3010	Metapillow breccia	Hyaloclastite
V550_165[b]	ODM165	13	18.846	−44	54.043	2885	Metapillow breccia	Hyaloclastite
V552_210	ODM210	13	19.365	−44	53.047	3228	Fault gouge with serpentinite fragments	Fault related
V553_227	ODM227	13	19.392	−44	54.454	2585	Mafic breccia	Undetermined
V553_228[b]	ODM228	13	19.334	−44	54.807	2515	Metapillow breccia	Hyaloclastite
V553_229	ODM229	13	19.421	−44	55.108	2489	Metapillow breccia	Hyaloclastite
V553_232	ODM232	13	19.433	−44	55.385	2479	Mafic breccia	Undetermined
V553_234	ODM234	13	19.451	−44	55.769	2490	Metapillow breccia	Hyaloclastite
V553_235	ODM235	13	19.483	−44	55.854	2497	Metapillow breccia	Hyaloclastite
V555_264	ODM264	13	19.306	−44	55.904	2466	Metapillow breccia	Hyaloclastite

[a]All mafic samples record greenschist conditions alteration.
[b]Sample with available thin section.

3. Methods

The microbathymetry, geological observations, and lithologies of the 13°20′N OCC used in this study were acquired during the ODEMAR cruise in 2013, onboard R/V Pourquoi Pas? (doi:10.17600/13030070; for details see *Escartín et al*. [2017]). The AUV Abyss (GEOMAR, Germany) was used to collect near-bottom microbathymetry data that allowed us to plan dives with the ROV Victor6000 (IFREMER, France), and select sampling targets for ROV dives or dredging. A total of 10 ROV dives were conducted at this detachment, with 5 of them over the corrugated fault surface itself (see ROV tracks in Figure 1b). In this study, we focus on a subset of the rocks recovered during ROV dives along this detachment surface that correspond to in situ sampling of the fault zone and that we link to high-resolution video imagery acquired during the ROV dives.

3.1. Video Observations and Videomosaics of Fault Outcrops

A primary objective of the five ROV dives conducted on the 13°20′N detachment fault surface was to investigate the nature of the microbathymetric corrugations, and of the detachment fault zone itself. These dives extended from the detachment's termination (hanging wall cutoff) to the limit of chaotic terrain off-axis (Figure 1b); both boundaries that are clearly defined in the microbathymetric data [*Escartín et al*., 2017]. While most of the detachment fault surface is pervasively covered with unconsolidated sediment and rubble, a total of seven fault plane exposures at the seafloor were identified during ROV dives [*Escartín et al*., 2017], all located on the flanks of microbathymetric corrugations (black circles in Figure 1b). Each outcrop was systematically video-surveyed with the high-resolution video cameras mounted on ROV VICTOR, and the imagery processed to generate geographically registered videomosaics [*Nicosevici and Garcia*, 2013]. Two of these videomosaics are shown in Figures 2b and 3b, and the remaining ones in supporting information Figures S1–S5.

3.2. Fault Rock Sampling and Reorientation

During ROV dives we recovered a total of 36 brecciated rock samples from the 13°20′N corrugated detachment surface. Eighteen of these were sampled from the exposed fault surfaces along the flanks of corrugations (Table 1 and Figures 2 and 3), and the remaining 18 were sampled ex situ from the unconsolidated sediment and rubble cover (Table 2). The onboard observations were reviewed onshore to determine the exact position of these samples in the corresponding outcrops and associated videomosaics (e.g., Figure 2 and supporting information Figures S1–S5). These data provide a detailed geological context for each sample studied here and allow us to determine that 14 samples were collected in situ from these detachment fault exposures (listed as in situ in Table 1). The remaining four samples were originally in situ, but dislodged

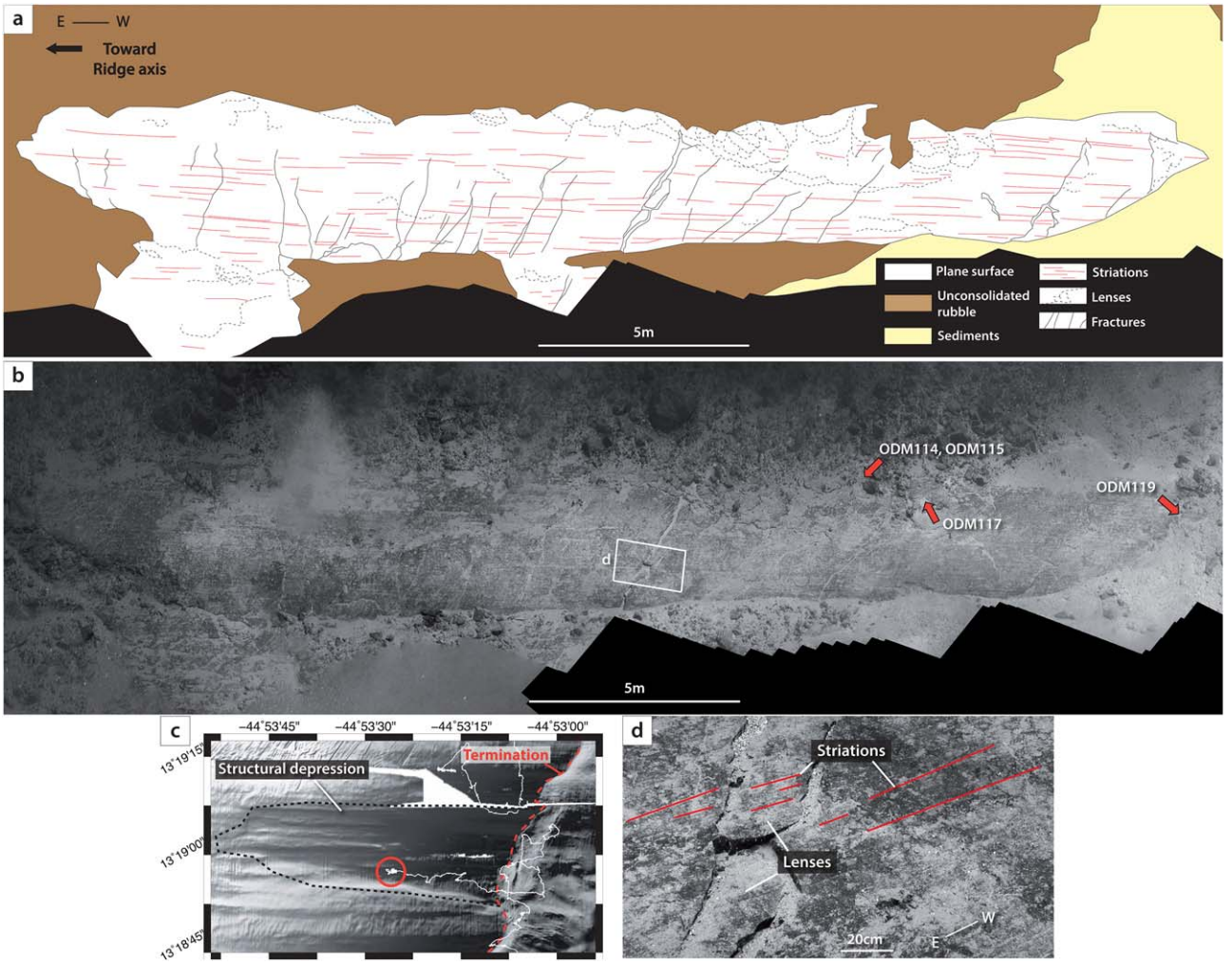

Figure 2. (a) Geological interpretation of (b) videomosaic ROV high-resolution video survey of outcrop #1 (see location in Figure 1b). Sample positions at this outcrop are indicated on (b) by red arrows and the sample name. (c) Shaded relief microbathymetry around outcrop #1 (red circle), which is located in a 70 m deep structural low (outlined by dashed line) with respect to the detachment fault surface (see also *Escartín et al.* [2017] for details). The termination (hanging wall cutoff) of the corrugated surface is shown with a dashed red line, and the ROV tracks with white lines. (d) Fault outcrops show planes that define lenses at scales of several centimeters to a meter wide. Subhorizontal, E-W striations (red lines) that are parallel to extension are widespread throughout the exposed fault surface.

from the outcrop and recovered in the immediate vicinity of their original position (these samples are listed as sub–in situ in Table 1). The video imagery of both the outcrop and the sample, in addition to visual examination of samples onboard and onshore, allowed us to identify their original location and orientation relative to the outcrop. We thus obtained absolute orientations using this visual information in combination with the corresponding ROV position, attitude (heading, pitch, and roll), and camera direction (pan and tilt). We estimate that sample orientations relative to the spreading direction are accurate within ~20°. Table 1 provides the location for all the samples.

3.3. Sample Preparation, Observations, and Mineral Analyses

All samples were cut on board to characterize their lithology and internal structure. Oriented samples were cut onshore in a direction parallel to spreading and perpendicular to it when possible. When the sample presents a fault plane, the cut surfaces are perpendicular to it (Figures 4, 5 and 9 and supporting information Figures S6–S9). Thin sections were prepared for all samples recovered along fault outcrops, as well as for a representative set of 8 out of the 18 ex situ samples collected on the sedimentary cover (samples indicated with an asterisk in Table 2).

Cut surfaces of in situ and oriented samples were digitally scanned and interpreted texturally at the sample scale (Figures 4, 5 and 10 and supporting information Figures S7–S9). Optical microscopy of thin-sections

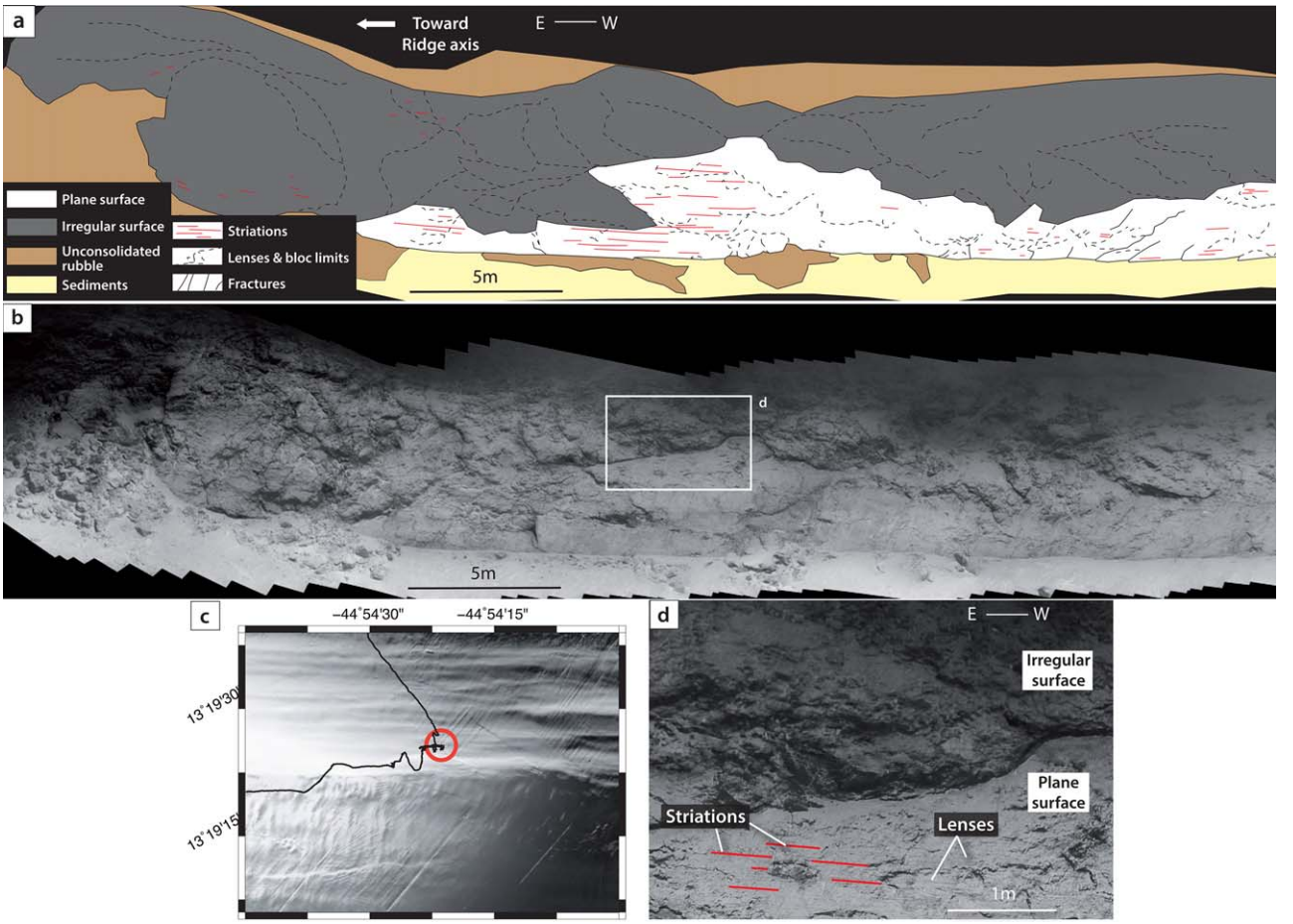

Figure 3. (a) Geological interpretation of (b) videomosaic ROV high-resolution video survey of outcrop #7 (see location in Figure 1b). (c) Shaded microbathymetry of outcrop #7 (red circle) with ROV tracks indicated by the black line. (d) The fault outcrop surface is irregular and shows lenses that display E-W striations. These striated planes are limited laterally and are located near irregular surfaces, and with planes defining large anastomosed blocks of fault rock.

was performed at Institut de Physique du Globe de Paris (IPGP, France) to identify the texture and mineral assemblages, and to assess the microstructure; an overview of the characteristics of each sample is given in Table 1. Scanning electron microscopy observations on representative samples were conducted on a SEM Zeiss Auriga equipped with EDS detector, also at IPGP, in addition to chemical analyses. Quantitative mineral analyses were obtained using an Electron Probe MicroAnalyzer EPMA (CAMECA SX-FIVE) at CAMPARIS (UPMC, Paris). In addition to the SEM observations, we also carried out cathodoluminescence microscopy using a SEM Zeiss Supra 55 (ISTeP UPMC, France) to study the structure and growth stages of crystals.

4. Results

4.1. Morphology and Structure of the Detachment at Fault Outcrops

Microbathymetric corrugations on the detachment surface correspond to anastomosing fault planes that are elongated parallel to the spreading direction [*Escartín et al*., 2017]. Detachment fault outcrops on the corrugated surface are distributed over ∼3 km in the along-axis direction (perpendicular to corrugations and spreading), and at distances from the termination in the extension direction of ∼1 km (#1 through #6, Figure 1b) to up to ∼3 km off-axis, near the summit of the corrugated surface (#7 in Figure 1b). While the corrugated surface is structurally continuous throughout with no late crosscutting faults [*Macleod et al*., 2009; *Escartín et al*., 2017], it shows a local structural depression near its termination, immediately south of the detachment center (see Figure 1b and details in *Escartín et al*. [2017]). This structural depression that extends 1.2 km parallel to corrugations and ∼0.6 km across has a maximum relative depth of ∼70 m and shows corrugations throughout. This structural low that corresponds to a missing portion of the

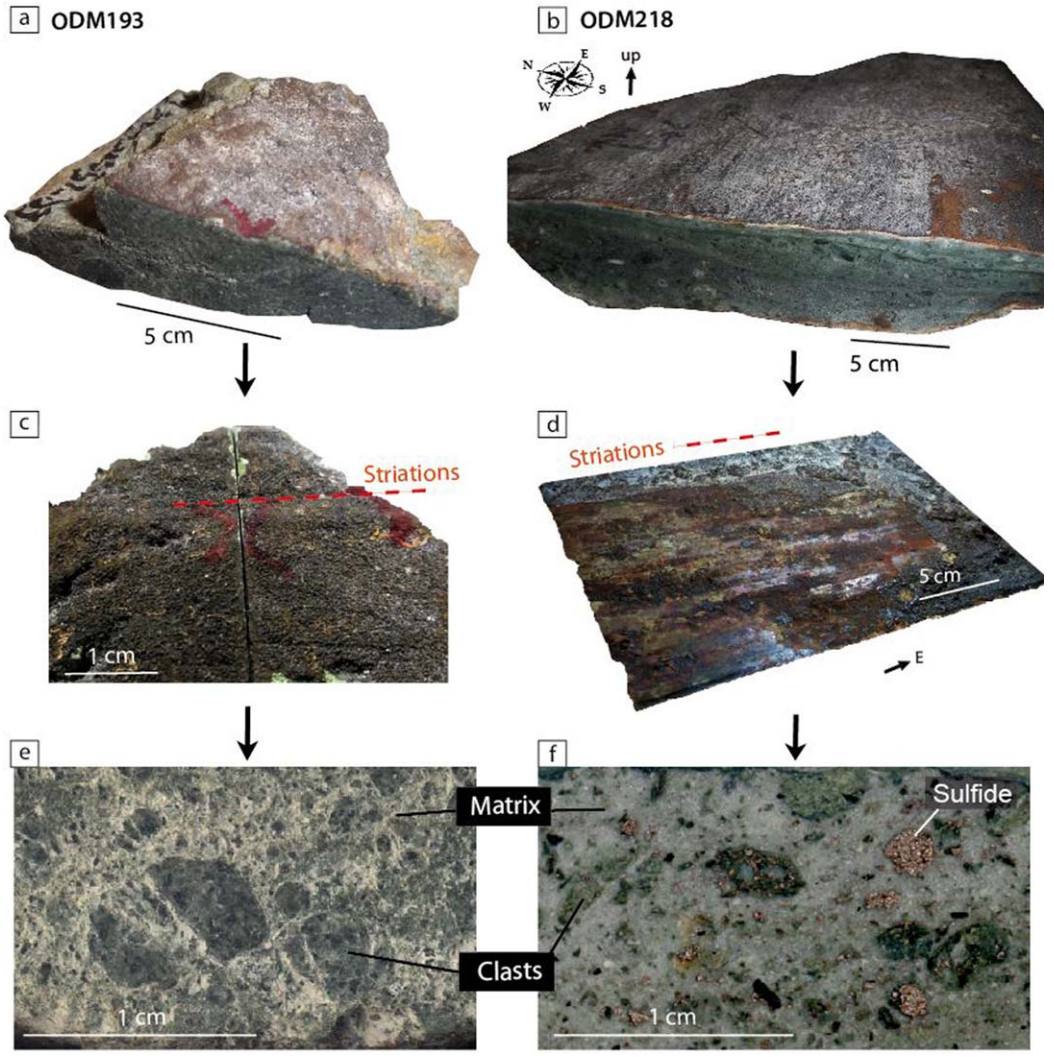

Figure 4. (a, b) Sample macrophotographs of two representative mafic fault rock breccias that have been cut perpendicular to extension (striation direction). ODM218 is oriented as indicated by the compass inset. Striations are observed both on the rough fault surface (c, ODM193) and on the smooth and reflective slip surface (d, ODM218). All breccias contain clasts of variable size and are either (e) clast-supported or (f) matrix-supported. In addition to the brecciated texture, (f) sample ODM218 contains sulfides.

detachment fault zone unequivocally demonstrates that the detachment fault zone has a thickness of at least 70 m and that the corrugations correspond to anastomosing fault planes controlling the internal detachment fault structure and its exposed surface [*Escartín et al*., 2017].

The detachment fault plane is ubiquitously covered with unconsolidated sediments and rubble. Outcrops of the detachment fault surface are systematically found on the flank of microbathymetric corrugations, where the greater slope has locally resulted in the shedding of the thin sediment cover, exposing the basement. These sediment and rubble-free fault planes typically dip up to 30° perpendicularly to spreading direction, and extend up to 90 m along the extension direction (see outcrops dimensions in Table 1 and Figures 2 and 3 and supporting information Figures S1–S5). Owing to the geometry, size, location, and continuity of the fault plane outcrops, and the consistency of tectonic structures at all scales (microbathymetry to outcrop and sample scales), we consider that these outcrops are unequivocally in situ and that they expose indeed the uppermost levels of the detachment fault zone at the seafloor. Additional detachment fault plane outcrops are likely to exist throughout the corrugated surface, primarily along the flanks of corrugations, as we infer the unconsolidated sediment and rubble cover to be thin (from ~1 to a few meters) based on ROV observations. As the 13°20′N detachment fault is not disrupted by late faults, the structural depression described above is the only

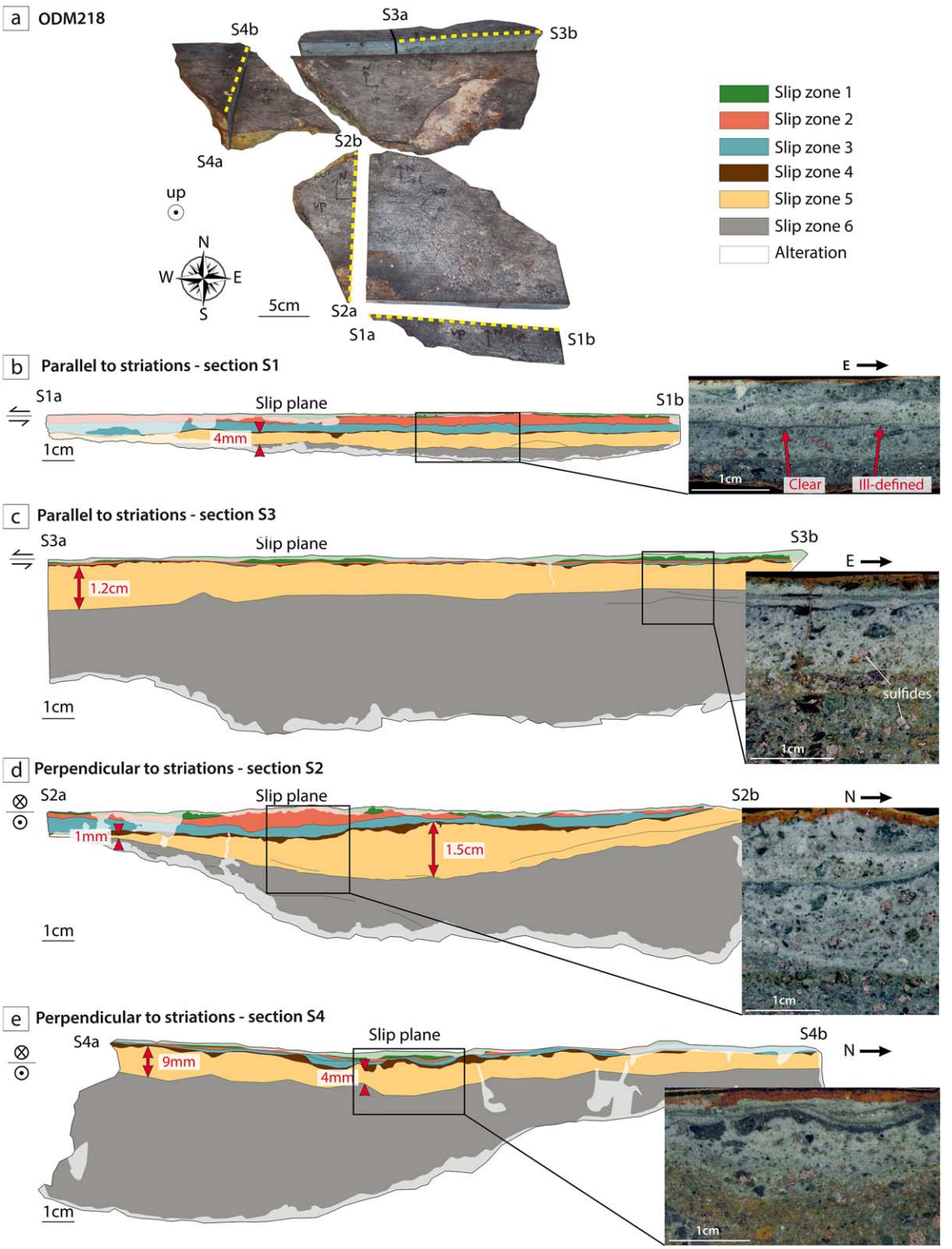

Figure 5. (a) Fault slab and associated fault slip plane (sample ODM218) that has been cut along four sections perpendicular to the slip plane: (b, c) two parallel to the striation direction, and (d, e) two perpendicular to it. (b–e) Interpretation of cut surfaces with detail of internal structures shown in the insets. The different slip zones observed macroscopically over the cut surfaces are distinguished by the different overall color, and clast content and size. Individual slip zones are indicated in the interpretations by different colors (slip zones 1 through 6). Internal structures within slip zones are outlined by black lines. To a first order, (b, c) slip zones are parallel to the striated surface and display relatively homogeneous thickness on the striation-parallel sections, whereas (d, e) their thickness is more variable along striation-perpendicular sections.

site that provides access to one outcrop (#1, Figures 1b and 2) that lies structurally ~50–70 m below the surrounding detachment surface, where the other six outcrops are found.

Examination of the videomosaics (Figures 2 and 3 and supporting information Figures S1–S4) reveals that the exposed fault planes have two distinct types of surface. We observe first that in five out of seven outcrops there are well-defined fault planes with subhorizontal striations up to 10 m long and subparallel to the spreading direction ("plane surfaces" in Figures 2 and 3 and supporting information Figures S1, S3, and S4). Close examination of these fault planes reveals a complex structure. Outcrops do not show a continuous fault plane. In some areas, they display small individual fault planes that terminate laterally against each other both along and across the extension direction. These fault planes define volumes of rock that are elongated in the extension direction with length scales that vary from ~1 m ("lenses" in Figures 2d and 3d and supporting information Figures S1e and S3d) to tens of meters (outcrop scale, Figures 2b and 3b and supporting information S1b, S3b, and S4b). In other areas, the fault outcrops display an irregular surface with anastomosing shear zones ("irregular surfaces" in Figure 3b and supporting information Figure S2a) that crosscut each other. These fault planes define rock lenses less than a meter thick, varying in length from a few tens of centimeters to several meters. Locally, these irregular surfaces show striations that do not exceed a few tens of centimeters in length and that are not laterally continuous at the outcrop scale (Figure 3d).

4.2. Detachment Fault Rocks

In this section, we first describe the 18 in situ and sub–in situ samples recovered along the fault outcrops (Table 1). They were recovered along both the well-defined and the irregular fault planes described in the previous section, and thus correspond to fault rocks from the detachment fault zone. All the rocks are cataclastic breccias, showing more or less penetrative deformation. In most of the samples, all the clasts are mafic. Only two (ODM173 and ODM217) contain ultramafic clasts in addition to mafic ones. For each fault rock type, we describe first the microstructures (from sample to microscale) and then the mineralogy. We also describe the 18 ex situ samples collected on the sediment cover (Table 2), and compare them with the in situ samples to understand their origin and position in the evolution and structure of the 13°20′N detachment fault.

4.2.1. Fault Rocks With a Mafic Protolith

4.2.1.1. Deformation Microstructures

The most widespread rock-type recovered from fault outcrops corresponds to variably silicified fault breccia that contains exclusively mafic clasts. Submilimetric to decametric clasts are observed in all studied samples, except for sample ODM115, which is itself a fault clast from ODM114. Clast content in these fault rocks is highly variable, both among samples and within a single sample, ranging from ~10 to 90 vol % clasts, resulting in textural heterogeneities. Two end-members are observed (see "texture" in Table 1): clast-supported breccias with more than ~60 vol % clasts (Figures 4a and 4e), and matrix-supported breccias with less than ~20 vol % clasts (Figures 4b and 4f). In both types of breccia, clast sizes are similarly heterogeneous and range from several cm to <1 mm. While clast size is variable, there is no apparent size or shape organization or sorting. Clasts are generally angular, particularly in clast-supported samples, and appear somewhat rounded in matrix-supported ones. The matrix, which lacks any internal structure, is fine-grained and is lighter in color than the larger clasts. The matrix of clast-supported breccias contains millimetric to submillimetric clasts (Figure 4e) resulting from cataclastic deformation. These small fragments are much rarer within the matrix-supported breccias where the matrix is fine-grained and shows a more homogeneous appearance to the naked eye (Figure 4f). A late network of chlorite veins is observed in two clast-supported breccia samples, ODM128 and ODM224. This network is poorly developed in ODM224, with the presence of only a few discontinuous and parallel veins, whereas it forms anastomosing cleavage domains spaced about 200 μm in sample ODM128 (supporting information Figure S6). This spaced cleavage isolates microlithons in which clasts are preserved (supporting information Figure S6d), indicating that the veining affected a rock already brecciated.

Macroscopically, most of these samples are slabs with either one or two flat surfaces (see "sample surface" in Table 1) that are parallel to the fault plane exposed on outcrops at the seafloor. From here on we refer to these zones where deformation localizes as *slip planes*. These slip planes flank *slip zones* resulting from penetrative deformation within cataclastic breccias, where the grain size is reduced. As described below and reported in Table 1, individual samples may show no, one, or two slip planes, and correspond to a single or contain more than one slip zones.

Figure 5 shows in detail the slip zones of sample ODM218 recovered from outcrop #2 (see Figure 1b for location). The nature and characteristics of the slip zones from this sample are representative of other mafic breccias found

in situ, that are therefore not described in detail here. ODM218 is a cataclastic breccia slab up to ~10 cm thick (Figure 4b), with a striated mirror-like fault surface (Figure 4d). Cuts perpendicular to the reflective surface, and both parallel and perpendicular to extension (Figure 5a) show up to five slip zones (Figures 5b–5e) whose average thickness is highly variable (a few mm to several cm). These slip zones are elongated parallel to extension, and their thickness variations are more pronounced across-extension (Figures 5d and 5e) than along the extension direction (Figures 5b and 5c). Slip zones closer to the slip surface are also thinner than those away from it, suggesting a link between their formation and the development of this slip plane. Boundaries between different slip zones can be either ill defined or sharp (see red arrows in Figure 5b). Sharp boundaries correspond to an abrupt change in texture (clast size and clast amount) and color, whereas boundaries that are not so well-defined are associated with a progressive change in color and texture instead (see insets in Figures 5b–5e). Both the abundance and size of the clasts vary among the different slip layers, with slip layers becoming more matrix-supported when close to the slip plane (see insets in Figures 5b–5e).

Slip planes display both grooves and striations in 10 of the in situ fault rock samples, as shown in Figures 4c and 4d. These planes were initially covered with a thin manganese crust that indicates a long-term exposure to seawater that was mechanically removed for sample observations. Systematically, these striations are subparallel to the extension direction, as observed for outcrop striations. In seven samples, the slip planes are reflective mirror-like fault surfaces (see Table 1, and sample ODM218, in Figure 4d). Grooves and striations are observed at different scales. The shortest striations show relatively high relief (up to ~1 mm) and lengths that do not exceed a few centimeters (Figure 4c). The longest striations are commonly observed on highly reflective mirror surfaces, and display low relief (<1 mm) forming elongated troughs up to 10 cm long (Figure 4d). In many instances striations initiate at pits and irregularities in the fault slip surface, indicating abrasion and/or trailing of material during fault slip, with a progressive decrease of the striation amplitude. This striation morphology is an indicator of the sense of deformation along these fault planes [*Doblas*, 1998], and all sample observations are consistent with westward movement of the detachment's footwall.

4.2.1.2. Textures and Mineral Assemblages

In the mafic fault breccias the petrological observations show that clasts are internally undeformed, and record variable degrees of hydrothermal alteration with a static replacement of primary minerals. The less altered clasts are systematically found in clast-supported breccias (Figure 4e). Found in all the in situ samples recovered from outcrop #4 (see Figure 1b for location), these clasts still display primary textures and minerals, and are therefore used to determine the primary lithology of the protolith. Primary minerals in clasts consist of fresh plagioclase (labradorite), and more rarely clinopyroxene, which shows crystals that are up to 500 μm long (Figure 6a). These clasts are surrounded by a matrix generally too fine-grained to be analyzed that contains fragments of clasts (Figure 6b). The relatively coarse-grained doleritic texture (Figure 6a) and the absence of altered glassy margins suggest that the protolith is not volcanic rock but diabase dyke.

In the weakly altered clasts, secondary amphibole is observed either in association with primary plagioclase, with albite, or alone (Figures 6a and 6b). These clasts may become chloritized with the replacement of plagioclase by chlorite and rare epidote, and amphibole by chlorite, in addition to the chloritization of the matrix. Quantitative analyses of amphibole have been carried out in four samples containing: (1) rare chlorite in the matrix and clasts (ODM193, ODM194, and ODM224), and (2) chlorite commonly found in both matrix and clasts (ODM195). They show an evolution in amphibole composition from hornblende to actinolite as a function of the increasing amount of chlorite (Figure 7). The mineral association in moderately altered clasts (plagioclase + hornblende) correspond to amphibolite conditions (≥500°C), whereas the paragenesis associated with chloritization (chlorite + albite + actinolite + epidote) correspond to greenschist conditions (300–400°C), indicating a progressive decrease of temperature of hydrothermal alteration as chloritization and associated silification (see next paragraph) become more widespread.

Primary minerals are either absent or very rare in the altered mafic fault rocks, due to efficient chloritization with the presence of variable amounts of titanite. Magmatic textures similar to those observed in the less altered samples described previously may still be visible in some chlorite clasts (supporting information Figure S10a) in mafic breccias from outcrops #2 and #6 (see Figure 1b for location). Therefore, we consider that these mafic breccias have a diabase protolith (Table 1). The fault clast ODM115 from outcrop #1 (see Figure 1b for location) shows the only occurrence of vacuoles indicating an extrusive origin among all the mafic breccia clasts examined from the in situ samples. For the remaining samples, no clear texture has been preserved to distinguish between a doleritic and an extrusive origin.

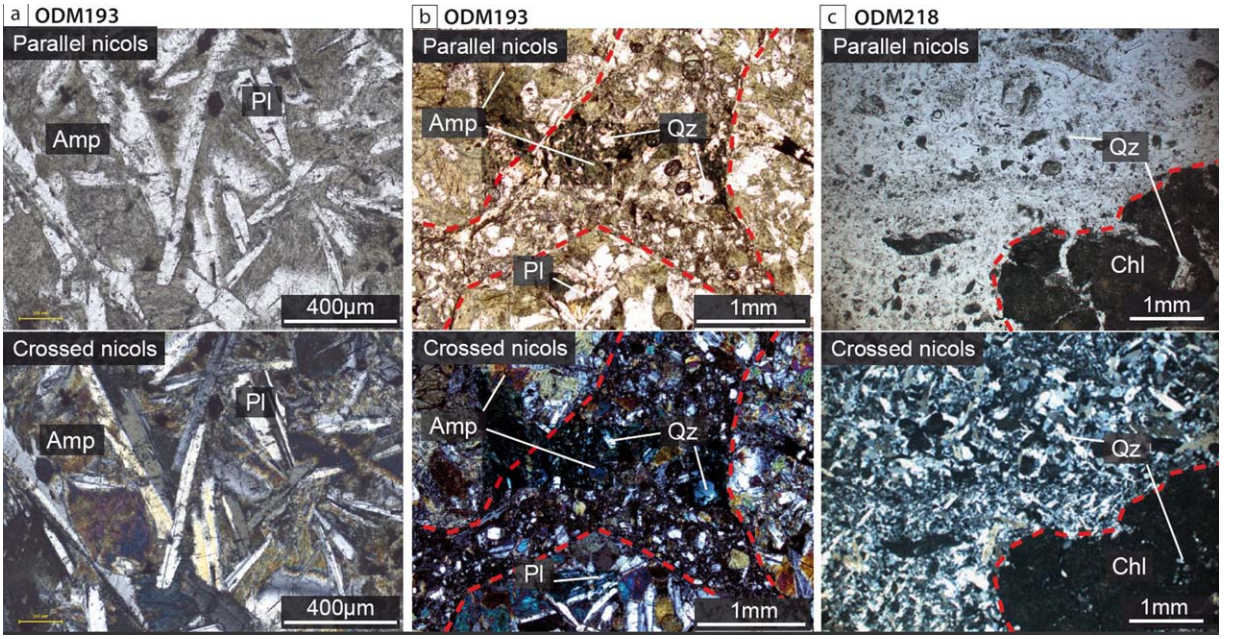

Figure 6. Optical microphotographs of mafic fault rock breccias parallel (top) and crossed (bottom) nicols. (a) The less altered clasts display a doleritic texture with unaltered magmatic plagioclase and hydrothermal amphibole. (b) Clast-supported breccias contain clasts of unaltered plagioclase and hydrothermal amphibole, surrounded by a fine-grained matrix containing additional rare quartz and chlorite. (c) Matrix-supported breccias display only fully chloritized clasts with variable amount of quartz, surrounded by a matrix mainly made of quartz with interstitial chlorite. Clast borders are indicated with red dotted lines. Mineral abbreviations: Amp, amphibole; Chl, chlorite; Qz, quartz; Pl, plagioclase.

Mafic breccias show silicification that varies from ~10 vol % quartz to almost complete silicification (>90 vol %). The *degree of silicification* related to the amount of quartz within a sample appears to correlate with sample texture, as it is systematically low to moderate for the clast-supported breccias and high for the matrix-supported ones. In moderately silicified mafic samples, quartz is exclusively found within the matrix and silicification is less than 10 vol %. Quartz grains grown with anhedral shapes are scattered in the matrix, or organized in local aggregates (Figure 6b). Highly altered fault rocks contain >90 vol % of quartz in the matrix, and in these samples clasts are also highly silicified (Figure 6c). Optical microscope observations (e.g., Figure 6c) show that the quartz grains display anhedral to subhedral crystal shapes. SEM observations (Figure 8a) show however the presence of irregular quartz grains next to subhedral grains. Chlorite is found either interstitially between quartz grains, or included in quartz grains as submillimetric fragments occasionally associated with amphibole (Figure 8a).

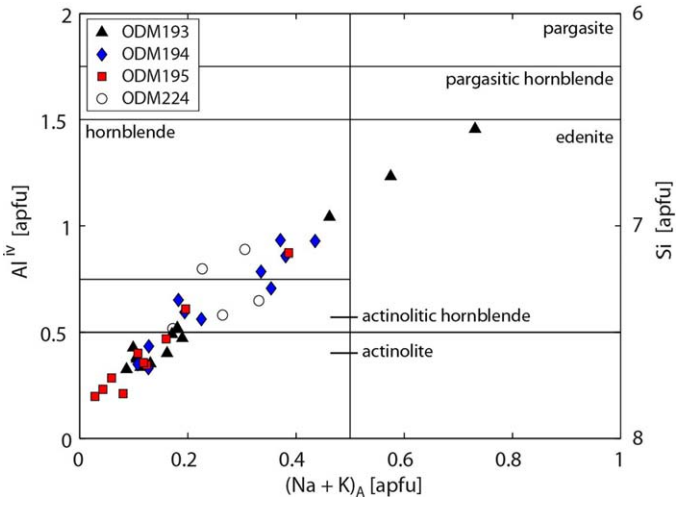

Figure 7. Composition of amphibole for four moderately silicified mafic samples containing rare chlorite in the matrix and clasts (ODM193, ODM194, and ODM224), and chlorite commonly found in both matrix and clasts (ODM195). The increase in chlorite contents is associated with a general shift toward amphibole compositions from hornblende to actinolite, corresponding to decreasing temperatures.

SEM-cathodoluminescence observations of quartz grains in three representative fault rocks (the moderately silicified ODM195 and the two highly silicified ODM155 and ODM218 mafic breccias, respectively 6, 21, and 14 quartz grains studied) reveal the presence of angular, fragmented cores surrounded by overgrowth or recrystallized rims (Figure 8b). Although interpretations are difficult as quartz grain borders might be

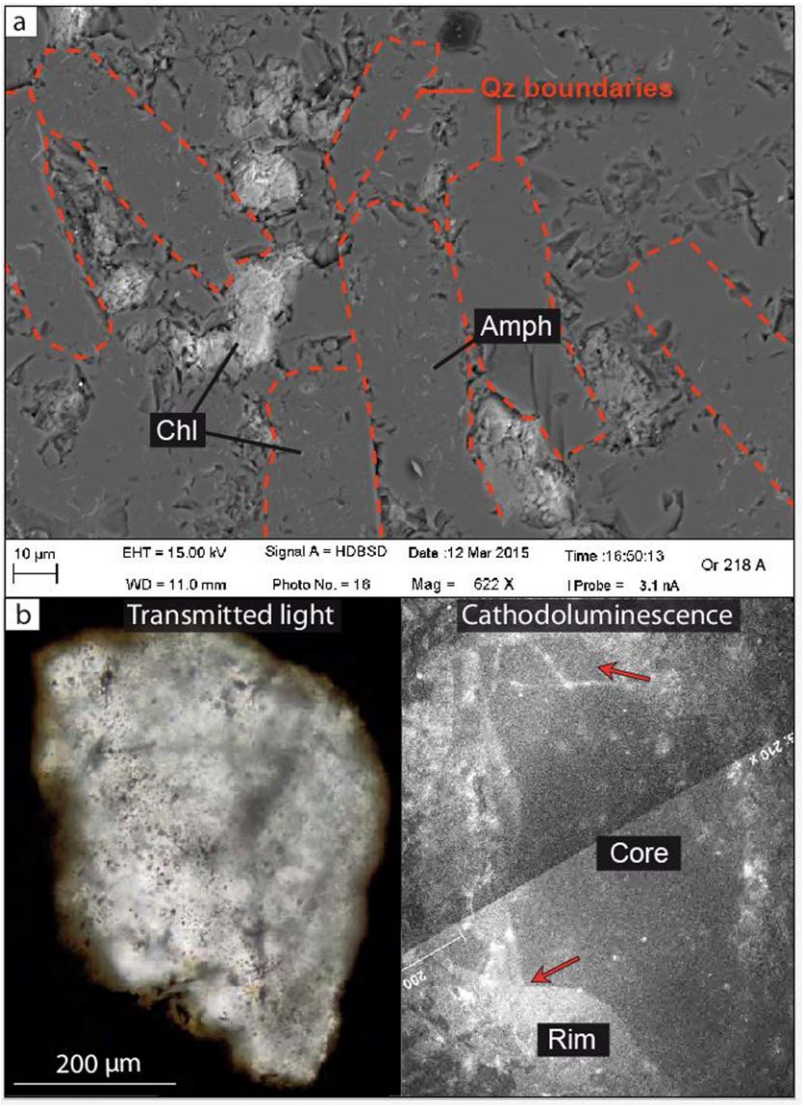

Figure 8. Morphology of quartz grains during (a) SEM and (b) SEM-cathodoluminescence imagery for ODM218. (a) Quartz grains displaying rod-like boundaries can be distinguished from irregular grains with unclear limits. Chlorite is found as an interstitial phase between quartz grains, and as submillimetric fragments together with amphibole within quartz grains. (b) SEM-cathodoluminescence images reveal that grains contain an angular and fragmented core (red arrows) surrounded by a recrystallized rim.

unclear, cathodoluminescence observations indicate that a large proportion of quartz grains have witnessed fracturing and subsequent crystal growth and (re)crystallization in highly silicified samples (66% for ODM155, 71% for ODM218), while such fractured grains are rare in the moderately silicified ODM195 (14%). These features illustrate successive generations of quartz crystallization and growth during silicification, and record quartz growth interrupted by fracturing events, particularly in highly silicified samples.

Sulfide mineralization is associated with silicification in the two highly silicified mafic fault rocks ODM155 and ODM218 (see "sulfides" in Table 1). Sulfides represent less than 1 vol % for each sample, and are uniformly disseminated in the matrix such as illustrated in Figure 4f. ODM218 contains mostly pyrite and pyrrhotite found as irregular crystals up to 2 mm in size (Figure 4f and insets in Figure 5), plus minor chalcopyrite intergrown with pyrrhotite. Pyrite is intricately linked to quartz, indicating that both minerals grew synchronously (supporting information Figure S10b). The amount of sulfide varies from one slip zone to another (see insets in Figure 5), and decreases toward the slip plane. In ODM155, the only sulfide is pyrite that occurs as crystals ranging from $\leq$1 to 5 mm in size. Similar to ODM218, the sulfide content varies from

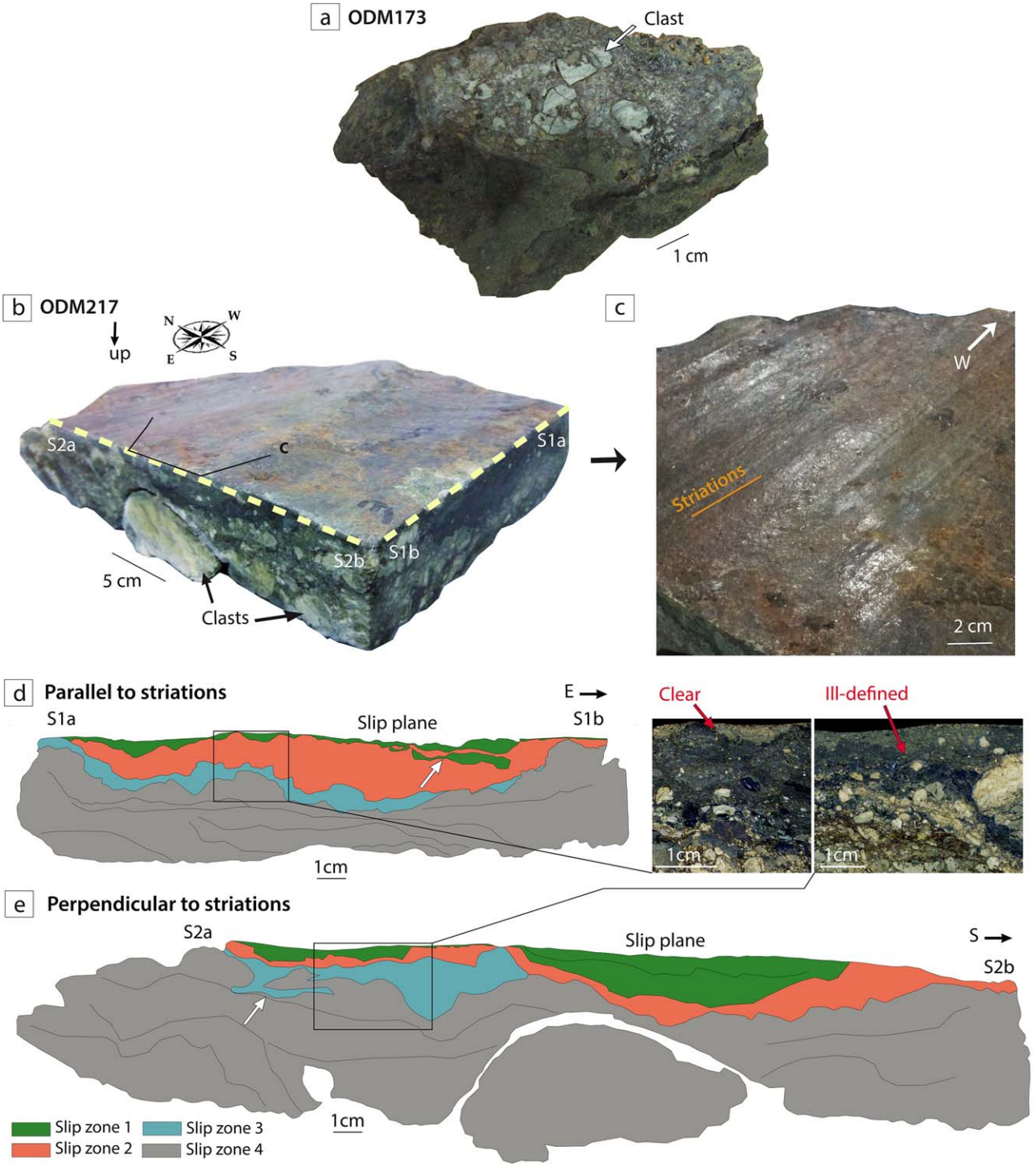

Figure 9. (a, b) Macrophotographs of the two fault rocks containing ultramafic material. (b) Location of the two sections of the oriented ODM217 fault rocks: (d) one parallel and the (e) other perpendicular to (c) striations. (d, e) Interpretation of cut surfaces whose structures are shown in the insets. Different slip zones are distinguished by their color and clast content. White arrows point to syn-deformation mechanical mixing between two layers. Internal structures are indicated by black lines. At first order, slip zones are parallel to the striated surface and have variable thicknesses along and across extension.

one slip zone to another and decreases toward the slip plane (insets in supporting information Figure S7). Additionally, ODM155 shows zones of pyrite mineralization that are deformed and elongated subparallel to slip zones (inset in supporting information Figure S7b).

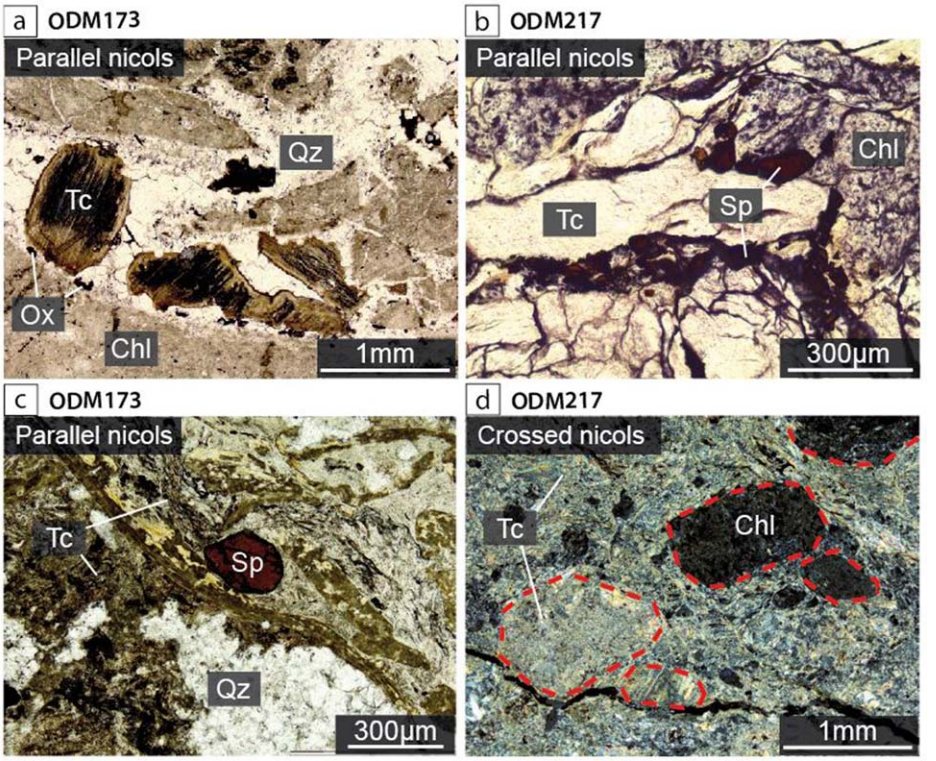

Figure 10. Photomicrographs under parallel and crossed nicols of the two fault rocks containing ultramafic material. (a) ODM173 records mark of hydrofracturing with the presence of quartz veins containing broken up clasts of talc. (b, c) The ultramafic component is suggested by the presence of talc and spinel in both rocks. (c) Quartz is widespread in the ODM173 matrix together with talc and chlorite. (d) Clasts of both talc and chlorite are commonly found in ODM217 (red dashed lines). Mineral abbreviations: Chl, chlorite; Ox, oxide; Qz, quartz; Sp, spinel; Tc, Talc.

4.2.2. Fault Rocks Containing Both Mafic and Ultramafic Protoliths

In this section, we describe two fault rock samples (ODM173 from outcrop #3 and ODM217 from outcrop #2, see Figure 1b for location) that contain ultramafic clasts in addition to the mafic ones. These outcrops also yielded breccias with only mafic clasts (described above).

4.2.2.1. Deformation Microstructures

The two samples containing ultramafic clasts are matrix-supported breccias with less than 40 vol % of clast content (Figures 9a and 9b). ODM173 shows two texturally distinct zones (Figure 9a): one with clasts up to 1 cm surrounded by a darker matrix, and the other more homogeneous under the naked eyes with clasts up to 1 mm. The transition between these two zones is gradual and extends over a thickness of few millimeters. Late quartz veins crosscut the breccia incorporating talc fragments, likely hydrofractured by the silica-rich fluids associated with the veining (Figure 10a). ODM217 contains millimetric to centimetric clasts (Figure 9b).

Of these two samples, only ODM217 displays a slip plane (Figure 9c) and slip zones (Figures 9d and 9e). Up to four slip zones can be distinguished at the sample scale by a change of color linked to a decrease of clast size and content toward the slip plane (Figures 9d and 9e). Slip zone thicknesses are in general more irregular and variable than those observed for mafic samples (Figure 5), but similarly, these variations are more important in sections cut across-striations (across spreading direction) than on the along-striations (Figures 9e and 9d, respectively). Moreover, slip zones are not continuous and may be truncated as observed for slip zone 3 in Figure 9d. Slip zone boundaries are either sharp or ill-defined and gradual, and their character may vary laterally (see insets in Figures 9d and 9e). In several instances these boundaries display small protrusions (e.g., slip zone 1 into slip zone 2, Figure 9d, and slip zone 3 into slip zone 4, Figure 9e), suggesting reworking and mechanical mixing after their formation.

The slip plane of ODM217, which was originally covered with a manganese crust indicating a long exposure to seawater at the seafloor, shows a reflective mirror surface with grooves and striations oriented East-West

(parallel to the spreading direction) similar to those described above (Figure 9c). These grooves and striations are elongated and up to 5 cm in length, <1 mm wide, with millimetric to submillimetric relief, and are similar to those observed in the pure mafic breccias described above (Figure 4d).

4.2.2.2. Textures and Mineral Assemblages

Both breccias show evidence for a mixing of ultramafic and mafic materials. Some of the clasts contain abundant talc, serpentine, and disseminated spinels (Figures 10b and 10c) that indicate an ultramafic origin. But others are made of chlorite with abundant titanite (Figures 10b and 10d) similar to those observed for the mafic breccias described above. The matrix is composed of fine-grained crushed fragments, associated with anhedral quartz crystals (<60 vol %) and few sulfides (<1 vol %) for ODM173 only (Figure 10c). Indeed, ODM173 is silicified while the matrix of ODM217 is quartz-free. Sulfides in ODM173 are chalcopyrite crystallizing along with quartz within the matrix, and pyrite occurring in late quartz-filled cracks. In both cases, the sulfide grains display irregular shapes and a size up to 1 mm.

4.2.3. Deformed Samples From the Detachment Rubble Blanket

Eighteen samples were recovered from the sediment and rubble covering the striated detachment fault surface (Table 2), and are therefore ex situ. To determine if these deformed rocks are similar to the in situ ones described above, and to understand their possible origin, we compare their composition and texture. Sixteen deformed samples have a mafic protolith (Table 2), one is a serpentinite gouge including serpentinite fragments (ODM210), and the last is a talc-schist (ODM150). Only one of the mafic breccias (ODM153, supporting information Figure S11a) shows a texture and composition similar to those found in situ and described above, and is thus interpreted as a fragment detached from the nearby fault zone. All other samples are texturally and/or mineralogically different from in situ samples, and therefore appear to have a different origin.

Indeed, 12 of the mafic ex situ breccias contain greenish angular pillow fragments with highly hydrothermally altered, variably thick glassy rims ranging from submillimeters to several centimeters in a fine-grained matrix with abundant altered small glassy shards (supporting information Figure S11b). These textures correspond to *hyaloclastites* (Figure 1b and Table 2) that result from fragmentation following sudden cooling and a thermal shock during rapid cooling and are unrelated to detachment fault deformation. Hyaloclastite clasts display pumpellyite aggregates in an assemblage of chlorite and quartz. Similar assemblages have been described in hydrothermally altered oceanic basalts [e.g., *Mével*, 1981; *Ishizuka*, 1999] and ascribed to seawater/rock interactions at temperatures consistent with prehnite-pumpellyite conditions (at ~250°C), which are somewhat cooler than greenschist conditions. The remaining three breccias show textures that are not clearly fault-related, and are referred to as *undetermined* in Table 2 (see also Figure 1b).

5. Discussion

The presence of in situ silicified mafic fault breccias has not been reported at oceanic detachment fault zones to date. To understand the nature and evolution of the 13°20′N oceanic detachment fault zone, its links to magmatic activity, its mechanical properties and mode of strain localization, and the origin of the rocks recovered, it is important to discuss the primary lithologies, the conditions of their hydrothermal alteration, and the relationship between deformation and silicification. Primary lithology and deformation processes operating within the fault zone, together with other geological and geophysical observations, also provide broad constraints on the geometry of the fault at depth and on its evolution. Here we discuss first the lithology and deformation microtextures at the detachment fault zone, and secondly the nature of the alteration fluids and the resulting silicification. Finally, based on these observations and results, we propose a history of detachment fault zone deformation and fluid circulation for the 13°20′N detachment, and compare this structure with other oceanic detachments.

5.1. Fault Composition, Structure, and Overplating With Hanging Wall Material

Hydrothermally altered diabase is the dominant lithology making up the cataclastic breccias of the oceanic detachment fault zone at the 13°20′N OCC (see "protolith" in Table 1). These breccias reach a thickness of at least 70 m near the detachment termination [*Escartín et al*., 2017]. There are two possible sources for these diabases, which are likely dyke fragments incorporated into the fault zone.

Dykes crosscutting or deformed in the fault zone have been observed at the 13°30′N detachment fault [*Escartín et al*., 2017], as well as at other OCCs [*MacLeod et al*., 2002; *Escartín et al*., 2003; *Blackman et al*.,

2006; *Dick et al*., 2008]. In these occurrences, diabase dykes are systematically associated with variably deformed ultramafic and/or gabbroic rocks that are the main lithologies of these fault zones. The presence of chill margins against fault rocks [*Escartín et al*., 2003; *Blackman et al*., 2006; *Dick et al*., 2008] indicates that diabase dykes are dykes crosscutting the heterogeneous detachment footwall lithosphere, probably injected into the active fault zone or emplaced after the fault related deformation event and that they are isolated and minor. In contrast, the 13°20′N detachment fault breccias contain almost exclusively diabase clasts, and their widespread occurrence throughout the detachment fault zone, both in the along and across-axis directions, precludes an isolated dyke origin for this material.

We suggest instead that these diabases originated from the dyke complex that likely forms the base of the upper crust of the hanging wall. In this area of the MAR, the rift valley floor shows a well-developed axial volcanic ridge, and the sonar acoustic backscatter shows a hummocky terrain indicating a pervasive volcanic cover, even though the reflectivity suggests that volcanic activity is less recent relative to adjacent rift valley floor both North and South of this OCC [*MacLeod et al*., 2009]. The volcanic nature of the rift valley floor is also confirmed by direct ROV observations of the seafloor during the ODEMAR cruise that documented pillow lavas and flat-topped seamounts abutting the detachment fault [*Escartín et al*., 2017], and by the extensive sampling of volcanic rocks throughout the rift valley floor [*MacLeod et al*., 2009]. The dyke complex from where the diabases may have originated is likely the feeder of these volcanics.

An origin from the base of the upper crust is consistent with the hydrothermal alteration of the diabase clasts. In breccias with low to moderate degrees of silicification, diabase clasts are characterized by the coexistence of hornblende and calcic plagioclase, i.e., amphibolite facies paragenesis ($\geq$500°C) (Figures 6a and 6b). This relatively high-temperature alteration is progressively overprinted by the development of abundant chlorite together with actinolite ($\pm$epidote) suggesting a decrease of the temperature (greenschist conditions) (Figure 7). Amphibole fragments in the matrix suggest that the high-temperature amphibolitization predates the tectonic brecciation and the incorporation of the clasts into the detachment fault zone. Similar mineral assemblages have been reported in the dyke complex drilled at Hole 504B [*Laverne et al*., 1995; *Alt*, 1995] and at Hole 1256D [*Alt et al*., 2010] from the Cocos-Nazca plate. Actinolite, albite, and chlorite secondary assemblages characterize the upper dyke complex, while hornblende becomes widespread in the lower dyke complex, at depths >1250 m into the basement. In metabasalts from the MAR near Kane, initial hydrothermal assemblages also vary from amphibolite conditions to greenschist conditions and are inferred to represent the upper and lower dyke complex, respectively [*Gillis and Thompson*, 1993]. Due to high heat flow combined with seawater penetration at the ridge axis, the upper oceanic crust displays a crude metamorphic layering ranging from low-temperature alteration at the surface, through zeolite and greenschist conditions, to amphibolite at the base of the dyke complex (see review in *Alt* [1995]). We therefore suggest that the fault sampled the dyke complex, hydrothermally altered at temperatures in the range of 500–300°C before being incorporated into the breccias. The highest temperatures are consistent with the "reaction zone" at the base of the convective hydrothermal cells [*Alt*, 1995].

Both outcrop observations and fault rock textures provide information on the nature and distribution of deformation within the detachment fault zone and suggest that deformation localizes along anastomosing shear zones over a wide range of spatial scales (km to cm). At outcrop scale, striated fault planes bound metric to decametric lenses of fault rock material (Figures 2 and 3 and supporting information S1–S5). At the seafloor scale, they define the surface of corrugations that extend over distances of $\sim$1 km or more in the spreading direction (Figure 1b) [*Escartín et al*., 2017]. Texture of fault rock samples documents strain localization on slip zones bounding bands of coarse-grained fault breccia that can be both clast-supported and matrix-supported by a fine-grain matrix (Figures 4, 5 and 10 and supporting information S7–S9). Away from the localized shear zones, deformation is penetrative and occurred under brittle conditions, resulting in brecciation of the rock (primarily mafic) and in the formation of a clast-supported breccia (Figure 4e). There is an apparent clast size decrease and matrix abundance increase toward the slip planes, with fault rocks becoming gradually more matrix-supported (Figures 4f and 5 and supporting information Figures S7 and S8), i.e., more cataclastically deformed. This suggests an increase of penetrative deformation and strain toward these slip planes.

We suggest that the deformation of mafic rocks from the hanging wall and their incorporation into the fault zone that is later exposed at the seafloor corresponds effectively to an overplating of the footwall with hanging wall material. This overplating involves primarily material from the dyke section at depth. With the

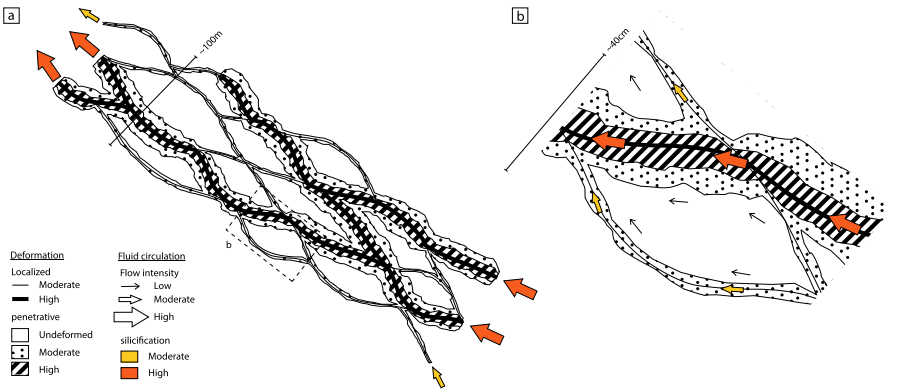

Figure 11. Sketch of the distribution of the deformation and fluid flow within the fault zone. (a) The fault zone is constituted of anastomosed blocks showing marks of localized deformation along their borders, and penetrative deformation toward their core. Heterogeneity in silicification and deformation observed in samples suggests also a variation in fluid flow intensity along different deformation zones and slip planes. (b) Close up at the scale of a fault block, showing details of the fluid flow and silicification.

exception of a single clast showing vacuoles (ODM115), the absence of clasts indicating a magmatic emplacement at the seafloor (glass rims, vesicles, hyaloclastic textures) also suggests that the basaltic material in the upper part of the hanging wall is not efficiently incorporated into the detachment fault zone. Although fault breccias contain mostly diabase clasts, local mixing with ultramafic clasts is also found (samples ODM173 and ODM217). The overplated material likely interacts with ultramafic material from the footwall in the fault zone. The fault zone is likely constituted of anastomosed blocks of various sizes with deformation heterogeneously localized on the block surfaces according to the preferential strain distribution (Figure 11). The differential displacements and transposition of the anastomosed blocks may generate the mixing of upper plate mafic dyke material with the underlying ultramafic material, as illustrated in Figure 12. While we have not sampled the footwall below the detachment fault directly in situ, abundant serpentinized peridotites and gabbros have been dredged from the detachment surface [*MacLeod et al*., 2009]. Furthermore, a footwall that contains both gabbro and/or peridotite has been suggested based on the interpretation of gravity data in the area [*Mallows and Searle*, 2012], and consistent with a heterogenous lithosphere, typical of slow spreading environments elsewhere [*Cannat*, 1993]. Therefore, ultramafic material

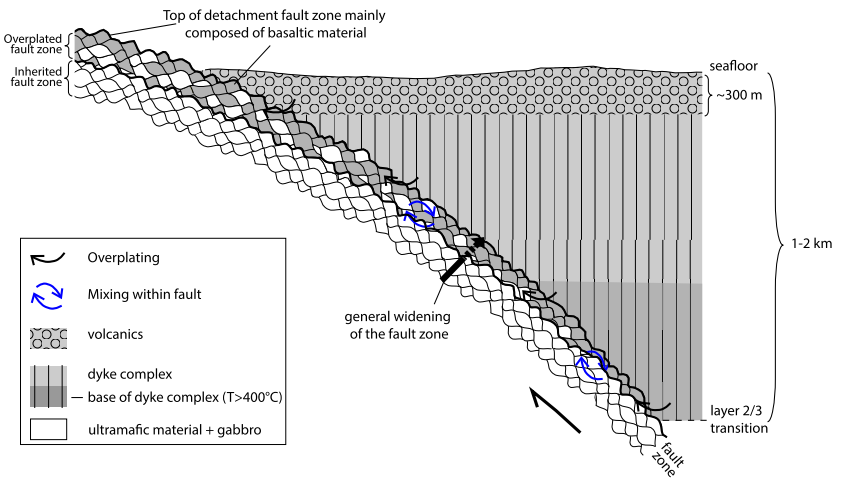

Figure 12. Schematic interpretation of the overplating of basalt/diabase material from the base of dyke complex (1–2 km below seafloor) into the detachment fault zone. This overplating may be due to the progressive migration of the fault into the hanging wall, resulting in a thickening leading to a general widening of the detachment fault zone from the base of dyke complex to its exhumation at the seafloor. This overplating is bound by the bold lines indicating the top of the detachment acting as the boundary between the hanging wall and the footwall (top bold line), and the bottom of the overplated fault zone (bottom bold line) overlying the former detachment, active at depths (below the mafic upper crust of the hanging wall). During the exhumation, internal deformation along the detachment fault zone, with anastomosing fault planes (Figure 11), can result in a local mixing of the underlying gabbro/peridotite fault material and the mafic hanging wall.

is likely uplifted by the 13°20′N detachment fault, as observed in other detachments, but it is not abundant at in the fault zone exposed at the seafloor owing to the incorporation of hanging wall material, and the development a primarily mafic upper fault zone that likely exceeds 70 m [*Escartín et al*., 2017]. This process of overplating takes place at depth from the base of the dyke complex diabase (under amphibolite conditions) to upper sections of the hanging wall crust (under greenschist conditions) but below the pillow section, as suggested by the lack of clasts corresponding to extrusive basalts (Figure 12), except for a single sample (ODM115).

Finally, the detachment fault surface is pervasively covered by unconsolidated rubble that appears to have been deposited at the termination and rafted with continued extension [*Escartín et al*., 2017]. In contrast with the fault rock material, most loose blocks are basaltic lavas with abundant glassy rims or fragments, sometimes hydrothermally altered. These differences clearly point to an upper crustal or surficial origin instead, further supporting their being sourced from mostly of extrusive basalts from the tectonically uplifted apron and the associated mass wasting along the hanging wall cutoff that covers the detachment surface with rubble [*Escartín et al*., 2017].

5.2. Silicification of the Detachment Fault

All the sampled detachment fault outcrops have yielded in situ rock samples that display variable degrees of silicification, indicating that these rocks have witnessed the circulation of Si-rich fluids and associated metasomatism. Systematic association of silica with chlorite of fault rocks, and its absence in the unconsolidated rubble overlying the detachment fault zone, demonstrates that the process of silicification occurred at depth, at a relatively high temperature around 300°C. Owing to this widespread occurrence of silicified in situ fault rocks throughout the detachment fault zone (Figure 1b) extending both along and across-axis, it is clear that the presence of silicifying fluids is not a local phenomenon that could be related to focussed discharge of fluids feeding vent fields.

5.2.1. Detachment Fault Deformation and Relationship to Silicification

At the regional scale, silicification is associated with deformation, and therefore with the fault movement and footwall exhumation. Our petrological and textural observations also indicate that the most deformed rocks, hence with more abundant matrix composed of crushed material, are the most silicified ones, also showing more pervasive chloritization (Figure 13). These observations clearly point to interactions between deformation and fluid flow (and associated alteration) that are complex and heterogenous at short spatial and temporal scales. These observations also point to a direct link between the intensity of deformation (and hence strain localization) and the amount of silicification, at the scale of individual shear zones and at the sample scale. This pattern suggests that the silica-rich fluids responsible for the crystallization of quartz were channelized into the shear zones at sample scale and that they reacted only moderately with the fault rock, even at small distances (cm scale) from the slip planes (Figure 11).

At the sample scale, however, microstructural and textural observations demonstrate that silicification postdates the formation of fault breccias and gouges. Examination of weakly to moderately silicified rocks (see "quartz content" in Table 1 and Figure 6b) suggests that silicification initiates with the formation of scattered quartz grains within the fault rock fine-grained matrix, and that it does not affect the associated clasts. In more silicified rocks (Figure 6c), the matrix shows abundant quartz that crystallized embedding submillimetric chlorite and relic amphibole fragments (Figure 8a). These observations suggest that a preexisting fault rock and its matrix (or former fault gouge) (Figure 13a) acts as both a fluid transport zone and a fluid-rock reaction zone that efficiently overprints the texture of the matrix supporting the fault breccia clasts.

The analysis of quartz textures and SEM-cathodoluminescence observations also indicate a complex link between deformation and the process of silicification. For example, sample ODM155 shows zones of pyrite mineralization that are elongated subparallel to fault slip zones and planes (supporting information Figure S6b), while sample ODM218 shows instead static sulfide growth (Figure 5). Similarly, the broken and recrystallized quartz grains revealed by SEM-cathodoluminescence imagery (Figure 8b) together with the fragments of reworked silicified matrix (Figure 13) demonstrate that the fault zone witnessed limited cataclastic deformation during the process of silicification.

The macroscopic and microstructural observations suggest, however, that quartz crystallization took place in the absence of any significant, overall deformation of these fault rocks, and that the observed brittle deformation of some of the quartz grains is likely associated with very small and/or local amounts of strain.

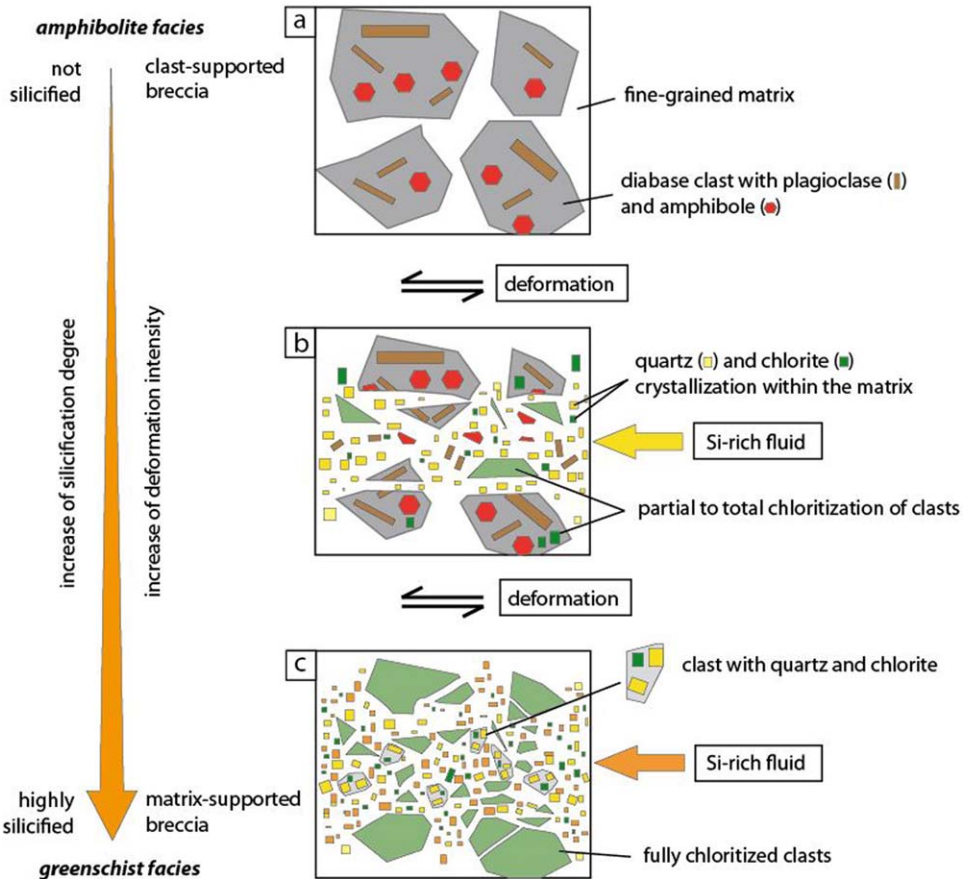

Figure 13. Proposed links and interaction between silicification and deformation along the 13°20′N detachment fault zone. (a) Prior to silicification, the clast-supported breccia contains plagioclase and amphibole both in clasts and disseminated within the fine-grained matrix. (b) The fault rock is deformed brittlely and with clast size reduction. After the deformation, quartz and chlorite crystallize within the matrix, together with a progressive chloritization of clasts. (c) Deformation continues to reduce the clast size and reworks the previously silicified matrix. Clasts are fully chloritized and silicification intensity of the matrix is highest.

In all the fault rocks examined the original, presilicification fault rock texture, with angular grains embedded in a matrix (Figure 5), is well preserved, and clasts do not show any apparent deformation (e.g., elongation of clasts) that would be expected of silicification occurring under deformation conditions. This is also confirmed by the examination of the original texture of clasts (Figure 6), that does not record any apparent deformation either. A detailed analysis of the slip surfaces, including fault mirrors, and the associated slip zones, including microstructural analyses, is out of the scope of this paper and will be the focus of a follow-up study.

These apparently contradictory observations (syntectonic and static silicification) can be explained by a syntectonic silicification at large spatial and temporal scales (overall development of the mafic fault zone at depth and subsequent exhumation). At smaller spatial and shorter temporal scales, silicification appears to be both pre and posttectonic, likely associated with the formation of individual fault deformation zones (Figure 11), and with zones of localized deformation along both internal slip planes and fault mirrors (Figures 5 and 9 and supporting information Figures S7 and S8). Indeed, when fluid is efficiently channelized into zones of localized deformation and/or high strain zones, pore fluid pressures may be elevated and may vary between lithostatic and hydrostatic depending on permeability and connectivity of the fault zone. These conditions can promote nonoriented static, euhedral quartz crystallization that can ultimately seal the fluid pathways locally. Increased fluid pressures can also produce the hydrofracturing, as suggested fractured and angular quartz grains that are subsequently recrystallized (Figure 8b).

We also note that our observations from the 13°20′N detachment fault zone exhumed at the seafloor demonstrate that strain localization is not facilitated by weak alteration minerals such as talc, serpentine and/or

chlorite, as suggested for other oceanic detachment faults [*Escartín et al*., 2003; *Shroeder and John*, 2004; *Boschi et al*., 2006; *Picazo et al*., 2012]. Instead, localized deformation along the striated fault planes that define the microbathymetric corrugations [*Escartín et al*., 2017] (Figures 2 and 3 and supporting information S1–S5) and the fault mirrors at sample scale (Figure 4d) involves both quartz and mafic material, that have much higher-friction coefficients [e.g., *Di Toro et al*., 2004; *Noda et al*., 2011]. This efficient strain localization suggests that factors other than the rheology of quartz and basalt (e.g., pore fluid and effective confining pressure, water weakening) are more important in controlling the effective friction along these deformation zones, and promote strain localization in the shallowest levels of the crust prior to the fault exhumation at the seafloor.

5.2.2. Origin of Silica

The presence of silica-rich fluids circulating along active fault zones is well documented in the oceanic lithosphere. The silica enrichment is inferred from fault rocks that are composed primarily of syntectonic talc, resulting in the widespread presence of talc schists at OCCs [e.g., *Escartín et al*., 2003; *Schroeder and John*, 2004; *Boschi et al*., 2006; *Dick et al*., 2008]. In ultramafic environments, silica is released into the fluid after pyroxene alteration according to the following reaction [e.g., *O'Hanley*, 1996; *Allen and Seyfried*, 2003; *Andreani et al*., 2007].

Orthopyroxene + water = serpentine + Si released in the fluid phase

$$3(Mg,Fe)SiO_3 + 2H_2O = (Mg,Fe)_3Si_2O_5(OH)_4 + SiO_{2(aq)}.$$

In ultramafic systems, silica appears to combine with serpentine and produce talc [e.g., *Frost and Beard*, 2007] with no quartz crystallization. Indeed, abundant quartz in association with talc schists has not been reported in any of these OCCs. As discussed before, although the 13°20′N fault rocks are composed mostly of mafic rocks overplated from the hanging wall, the footwall is probably of heterogenous nature and contains serpentinized peridotites. Recovered ultramafic rocks are predominantly undeformed serpentinized harzburgites [*Escartín et al*., 2017] and contain enough orthopyroxene to potentially release substantial amounts of silica that can be taken up by fluids. But this does not satisfyingly explain the absence of quartz at other oceanic detachment fault zones.

Alternatively, the alteration of basaltic rocks could be an additional source for silica. Basalt-water interaction experiments [*Mottl*, 1983] have shown that quartz-chlorite-oxide assemblages replace basalts at 300°C and high water-rock ratios. Thermodynamic models based on reaction paths at 300°C using the average Atlantic N-MORB composition [e.g., *Bach et al*., 2013] yield mineral assemblages consistent with these experimental studies. Rocks containing chlorite and quartz also occur in natural oceanic environments. They have been locally reported from the transition zone between sheeted dykes and lava flows in drill Hole 504B [*Honnorez et al*., 1983; *Alt et al*., 1986, 1996]. Quartz associated with chlorite occurs also in metabasalts from the MAR [*Humphris and Thompson*, 1978; *Gillis and Thompson*, 1993]. Quartz-chlorite breccias have been sampled at the base of the eastern valley wall of the MAR near Kane area [*Delaney et al*., 1987] in the vicinity of metadiabases, therefore probably associated with dykes. Drilling of the TAG hydrothermal field has also shown the presence of silicified and choritized basaltic wall rocks in the shallow root of the mound [*Humphris et al*., 1996], indicating that silica rich fluids are generated in the reaction zone and discharged beneath the active vents. Formation of silica-rich fluids in the lower dykes and uppermost gabbros have been documented at Hole 504B [*Honnorez et al*., 1983; *Alt et al*., 1986, 1996], Hole 1256D [*Alt et al*., 2010], and Pito Deep [*Heft et al*., 2008]. Under particular conditions these fluids may focus and flow upward to sustain local hydrothermal fields at the seafloor (i.e., TAG).

The fact that intensely silicified fault breccias have been described so far only at 13°20′N, in association with mafic rocks overplated from the hanging wall, seems to be more consistent with silica-rich fluids produced by basalt-seawater alteration. Interaction between the fault and the overhanging plate can promote near-fault damage [*Cannat et al*., 2009] of the hanging wall, locally increasing the permeability and favoring high-water rock ratios necessary to silicified mafic rocks. Silica-rich fluids produced at depth can then be channelized into the detachment fault zone when it penetrates the reaction zone at the base of the dyke complex. This would allow not only to overplate material from the hanging wall but also to produce the massive silicification associated with deformation. However, we cannot preclude a mixing between these basalt-derived fluids and silica-rich fluids generated by serpentinization of the footwall that is inferred to include ultramafic materials [*Mallows and Searle*, 2012].

5.3. Fault Geometry at Depth and Link to Axial Processes

To understand how the fault operates and to determine how the different processes of deformation and alteration described above are related to the detachment evolution and where they may occur, the subseafloor geometry of the 13°20′N is an important parameter. Lacking direct geophysical constraints, here we discuss both observations from this area and a comparison with studies of other detachment fault systems that may provide insight into fault geometry at depth.

The elevated seismicity rates of the ridge section at both the 13°20′N and 13°30′N OCCs are similar to those at other detachment-bearing MAR ridge sections [*Escartín et al*., 2008], such as TAG [*Kong et al*., 1992; *deMartin et al*., 2007], Logatchev [*Grevemeyer et al*., 2013], or 23°N [*Toomey et al*., 1985]. Microseismic experiments at these sites show a maximum depth of seismicity at 6–8 km below seafloor that may also coincide with the deepest extent of the detachment fault below the rift valley floor. This maximum seismicity depth may also be a proxy for the brittle-to-plastic transition at around ∼750°C [*Kohlstedt et al*., 1995], also interpreted as the base of localized brittle (seismogenic) deformation and hence of detachment faulting.

Both the curvature in the along-extension direction of the detachment fault surface exposed at the seafloor, which is extremely regular, and the angle of this fault at the detachment hanging wall cutoff, can also be used to infer fault geometry at depth. The fault curvature can be fit with circles that have diameters of ∼9 to 11 km. The TAG detachment fault dip of 70° at depth is inferred from microseismicity [*deMartin et al*., 2007], consistent with a curved fault geometry required to explain footwall rotations for ∼35° to 45° from paleomagnetic studies [*MacLeod et al*., 2009; *Morris et al*., 2009]. Using a fault radius of ∼9–10 km (Figure 14), we obtain a ∼70° fault dip at ∼5 km or deeper below seafloor, consistent with the range of depths for the base of microseismicity at other sites (6–8 km).

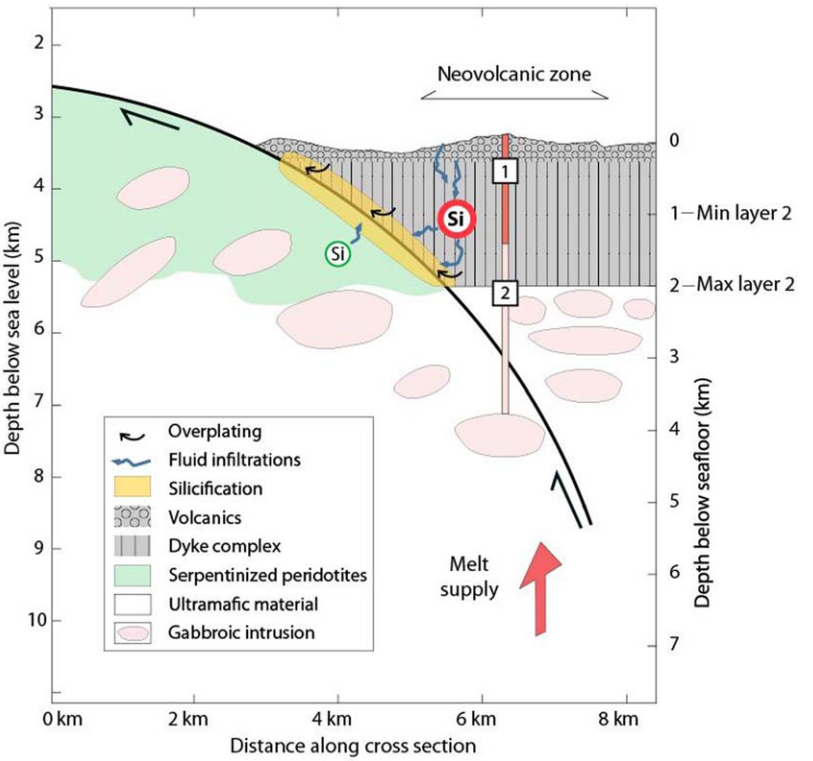

Figure 14. Cross section (no vertical exaggeration) depicting the inferred internal structure of the 13°20′N detachment fault at depth, and its interaction with the magmatic hanging wall. The plain bold curve corresponds to a curvature of 9 km of radius. Detachment faults are believed to initiate at ∼70° [*MacLeod et al*., 2009], giving for this model a depth of about 5 km. The upper crust is estimated to range between 1 and 2 km in thickness, lacking further geophysical constraints (see discussion in text). The magmatic supply for the neovolcanic zone can be related to lateral dyke propagation (in orange and labeled "1") or to dyke intrusions (in pink and labeled "2"). Silica can be extracted from ultramafic material after serpentinization reactions (minor release), or it can be release after alteration of the basalt/diabase material from the hanging wall (major release). Silica is then channelized by the permeable fault zone, and controlled by the internal structure (see Figure 12), leading to quartz precipitation.

We have no direct constraints for this area on the thickness of the basaltic upper crustal layers at the hanging wall, although this is an important parameter to determine the location of the deepest, hydrothermally altered diabase levels that deformed and incorporated into the detachment fault zone together with hydrothermal silica-rich fluids (Figure 12). Direct information on the extrusive pile and the layer 2 thicknesses has been documented by drilling in fast spread crust generated at the Costa-Rica rift. In Hole 504B, the transition between the lavas and the dyke complex starts around subbasement depths of 600 m, while hydrothermal alteration yielding secondary hornblende occurs in the lower dyke complex, i.e., between 1500 and 2000 m [*Alt et al*., 1996]. In the nearby IODP Hole 1256D drilled in ultrafast spread crust, the lava-dyke transition starts at ~1060 m, hornblende occurs below ~1350 m, and the dyke-gabbro transition is encountered at ~1400 m [*Wilson et al*., 2006]. This shows that the thickness of layer 2 varies from 1400 to >2000 m, possibly depending on the spreading rate, but that high-temperature (~500°C) hydrothermal alteration is reached at depths of 1300–1500 m. Unfortunately, there is no such direct information for slow spreading ridges. Seismic refraction experiments elsewhere along the MAR and near oceanic detachments show a layer 2 thickness that ranges from ~1 to 2 km. For example, for the axial crust near the rifted 5°S detachment, *Reston et al*. [2002] report a layer 2 thickness of ~1 to 2 km, while near the 23°N detachment, *Dannowski et al*. [2010] report a thickness of 1.5–2 km. These layer 2 thicknesses are not very different from the 1–2 km reported along a more magmatic MAR ridge segment at 35°N [*Canales et al*., 2000; *Hooft et al*., 2000]. Although the thermal structure and the magma budget is different from fast spreading ridges, there does not seem to be a striking difference in the layer 2 thickness. Based on these results, we use in Figure 14 an extrusive axial thickness that may vary between 1 and 2 km.

This fault geometry suggests that the overplating of mafic material into the fault zone is thus a relatively shallow process that can only be initiated 1–2 km below the seafloor at temperatures of ≥300°C, as discussed above. Based on the curvature of the fault (Figure 14), detachment fault dip at the contact with the base of the diabase layer is likely to be lower than 45°. Moreover, the deeper sections of the detachment fault zones likely operate at temperatures >300°C and up to 500°C, based on the hydrothermal alteration recorded in the clasts within the fault rocks.

This inferred fault geometry also suggests a complex and yet unconstrained interaction between the deeper magmatic system feeding the rift valley floor volcanics and underlying diabases, and the detachment fault itself. Based on sonar data interpretations and dredge results, *Macleod et al*. [2009] suggested that volcanics at the ridge valley floor adjacent to the detachment may source from laterally propagating dykes (heat source #1 in Figure 14), with magma sources located either to the North and the South of the detachment. Alternatively, these volcanics may be fed vertically from underlying magma chambers emplaced within the footwall (heat source #2 in Figure 14). The interactions between the active detachment fault and the dyke system is likely for each of these scenarios, but it is not constrained lacking additional geophysical data. Such heat sources at depth may also sustain the present-day, high-temperature Irinovskoe hydrothermal field (location in Figure 1b).

Although other oceanic detachments show adjacent volcanic seafloor within the rift valley, none of them show incorporation of mafic rocks from the hanging wall into the fault zone. Possible factors that may contribute to diabase overplating and associated silicification include the geometry of the deformation zone (fault dip and thickness of the dyke section), the temperature and pressure (fluids, depth) conditions, the permeability of the overhanging plate that may or may not allow the formation of silica-rich fluid in the reaction zone at the base of the dyke complex and their release in the fault zone. All these factors may control strain localization, fault strength, and ultimately the migration of the zone of deformation into the hanging wall required for overplating with hanging wall material. Neither our results nor existing data provide enough information to determine why overplating is operating in our study area and not at other detachments. Additional constraints are required to understand how this system operates. Fluid inclusions trapped in quartz crystals from silicified zone are currently being studied and will bring additional information on the silica-rich fluids and the conditions of silicification [*Bonnemains et al*., 2016], and will be presented in a future paper. Moreover, both an active and passive seismic experiment was recently conducted in the area [*Reston et al*., 2016], whose results will provide further constraints on lithospheric structure and fault geometry at depth, and therefore on the processes discussed here.

6. Conclusion

We have conducted a textural, mineralogical, and microstructural study of 18 fault rock samples recovered in situ with a remotely operated vehicle along the detachment fault zone of the 13°20′N oceanic core

complex at the Mid-Atlantic Ridge. The exposed detachment fault surface at the seafloor shows a corrugated fault surface, with striated fault outcrops on flanks of individual corrugations that have been sampled for this study. Field observations and sampling demonstrate that the bulk of the detachment fault zone exposed, with a thickness of ~70 m, is composed almost exclusively of mafic fault breccias with the occurrence of only two breccias samples with mixed ultramafic and mafic clasts. All samples display silicification of varying intensity linked to the detachment fault deformation. The least silicified rocks show mafic clasts hydrothermally altered under amphibolite to greenschist conditions. The primary mineral assemblages, the coarse mineral grains in clasts, and the absence of former glassy textures indicate a diabase protolith for these breccias. Fully silicified breccias show quartz precipitation both in matrix and clasts.

At the sample scale, these fault rocks display both penetrative deformation (fault breccia), and localized deformation (along internal slip planes and surface fault mirrors, often striated), and may record several slip events within a single sample. We also document a complex history of silicification. The most deformed samples are also the most silicified, showing a strong relationship between deformation and silicification. Quartz crystals show both evidence of crystallization under static conditions, with no preferred lattice orientation, and under deformation or reworked by clastic deformation, with broken up and recrystallized grains. Silicification may postdate the brecciation event as deformation textures are preserved and subsequently silicified. However, localized deformation along fault slip planes and fault mirrors also generate grooves and striations at the surface of already silicified rocks. These observations record a complex interaction between deformation (both localized and penetrative) and silicification at short temporal and spatial scales within and active detachment fault zone.

A fault zone mainly composed of cataclastic metadiabase breccias is the first observation of this kind in an oceanic detachment fault that elsewhere are dominated by gabbros and peridotites, more or less deformed and recrystallized, in addition to limited amounts of basaltic material. The source of the widespread mafic fault rocks is likely the base of the magmatic upper crust in the hanging wall under the volcanic rift valley seafloor, and at depths consistent with amphibolite to greenschist facies hydrothermal alteration. This implies that the hanging wall material near the detachment fault is deformed, incorporated into the fault zone, and ultimately accreted to the footwall. These overplated metadiabase breccias likely overly a fault zone penetrating into "typical" gabbroic and ultramafic material, as suggested by the two mixed breccias (mafic and ultramafic clasts) presented here. This material likely originates from the footwall made up of heterogeneous lithosphere typical of slow spread environments. These results also demonstrate that extreme strain localization is also achieved in the absence of weak alteration phases such as talc and serpentinite, and involving higher-friction materials (quartz and diabase), suggesting that elevated pore fluid pressures play a role.

Acknowledgments

We thank the officers, crew, and technical staff onboard R/V Pourquoi Pas? During the ODEMAR cruise for their efforts and dedication that allowed us to collect the data and samples presented here. The authors thank Nuno Gracias and Ricard Campos for the videomosaics of fault outcrops, and B. John and L. Labrousse for fruitful discussions and comments. We thank J. Alt and N. Hayman for thoughtful comments. The data used are listed in the tables and supporting information. Ship and ROV time, as well as funds for cruise support and postcruise science, were granted to the PIs (JE and MA) by IFREMER, and CNRS/INSU. D. Bonnemains and J. Escartín were also supported by the DCO initiative from the Alfred Sloan Foundation, and an INSU-SYSTER grant to JE and MA provided support for analytical and microscopic work. This project benefitted from no ANR (France) support. This is IPGP contribution #3843.

References

Allen, D., and W. Seyfried (2003), Compositional controls on vent fluids from ultramafic-hosted hydrothermal systems at mid-ocean ridges: An experimental study at 400°C, 500 bars, *Geochem. Cosmochim. Acta*, *67*, 1531–1542, doi:10.1016/S0016-7037(02)01173-0.

Alt, C. J. (1995), Subseafloor processes in mid-ocean ridge hydrothermal systems, in *Seafloor Hydrothermal Systems: Physical, Chemical, Biological, and Geological Interactions, Geophys. Monogr. Ser.*, vol. 91, edited by S. E. Humphris et al., pp. 85–114, AGU, Washington, D. C., doi:10.1029/GM091p0085.

Alt, C. J., J. Honnorez, C. Laverne, and R. Emmermann (1986), Hydrothermal alteration of a 1 km section through the upper oceanic crust, deep sea drilling project hole 504B: Mineralogy, chemistry, and evolution of seawater-basalt interactions, *J. Geophys. Res.*, *91*, 10,309–10,335, doi:10.1029/JB091iB10p10309.

Alt, J. C., C. Laverne, D. Vanko, P. Tartarotti, D. A. H. Teagle, W. Bach, E. Zuleger, J. Erzinger, and J. Honnorez (1996), Hydrothermal alteration of a section of upper oceanic crust in the eastern equatorial Pacific: A synthesis of results from DSDP/ODP Legs 69, 70, 83, 111, 137, 140, and 148 at Site 504B, in *Proceedings of the Ocean Drilling Program Scientific Results*, vol. 148, pp. 417–434, Ocean Drill. Program, College Station, Tex.

Alt, J. C., C. Laverne, R. M. Coggon, D. A. H. Teagle, N. R. Banerjee, S. Morgan, C. E. Smith-Duque, M. Harris, and L. Galli (2010), Subsurface structure of a submarine hydrothermal system in ocean crust formed at the East Pacific Rise, ODP/IODP Site 1256, *Geochem. Geophys. Geosyst.*, *11*, Q10010, doi:10.1029/2010GC003144.

Andreani, M., C. Mével, A. M. Boullier, and J. Escartín (2007), Dynamic control on serpentine crystallization in veins: Constraints on hydration processes in oceanic peridotites, *Geochem. Geophys. Geosyst.*, *8*, Q02012, doi:10.1029/2006GC001373.

Bach, W., N. Jöns, and F. Klein (2013), Metasomatism within the ocean crust, in *Metasomatism and the Chemical Transformation of Rock: The Role of Fluids in Terrestrial and Extraterrestrial Processes, Lect. Notes Earth Syst. Sci.*, pp. 253–288, Springer, Berlin Heidelberg, doi:10.1007/978-3-642-28394-9.

Beltenev, V., et al. (2003), New discovery at 12°58′N, 44°52′W, MAR: Professor Logatchev-22 cruise, initial results, *InterRidge News*, *12*, 13–16.

Beltevev, V., et al. (2007), A new hydrothermal field at 13°30′N on the Mid-Atlantic Ridge, *InterRidge News*, *16*, 9–11.

Blackman, D. K., J. R. Cann, B. Janssen, and D. K. Smith (1998), Origin of extensional core complexes: Evidence from the Mid-Atlantic Ridge at Atlantis fracture zone, *J. Geophys. Res.*, *103*, 21,315–21,333, doi:10.1029/98JB01756.

Blackman, D. K., B. Ildefonse, B. E. John, Y. Ohara, D. J. Miller, C. J. MacLeod, and the Expedition 304/305 Scientists (2006), *Proceedings of the Integrated Ocean Drilling Program*, vol. 304/305, Integrated Ocean Drill. Program, College Station, Tex., doi:10.2204/iodp.proc.304305.2006.

Bonnemains, D., A. Verlaguet, J. Escartín, C. Mével, and M. Andreani (2016), Hydrothermal circulation along oceanic detachment fault: Constraints on the nature and conditions of syntectonic silicification at the 13°20′N oceanic core complex (Mid-Atlantic Ridge), Abstract A14B-1234 presented at AGU Fall Meeting, AGU, San Francisco, Calif., 12–16 Dec.

Boschi, C., G. L. Früh-Green, and A. Delacour (2006), Mass transfer and fluid flow during detachment faulting and development of an oceanic core complex, Atlantis Massif (MAR 30°N), *Geochem. Geophys. Geosyst.*, *7*, Q01004, doi:10.1029/2005GC001074.

Buck, W. R., L. L. Lavier, and A. N. B. Poliakov (2005), Modes of faulting at mid-ocean ridges, *Nature*, *434*, 719–723, doi:10.1038/nature03358.

Canales, J. P., R. S. Detrick, J. Lin, and J. A. Collins (2000), Crustal and upper mantle seismic structure beneath the rift mountains and across a nontransform offset at the Mid-Atlantic Ridge (35°N), *J. Geophys. Res.*, *105*, 2699–2719, doi:10.1029/1999JB900379.

Cann, J. R., D. K. Blackman, D. K. Smith, E. McAllister, B. Janssen, and S. Mello, E. Avgerinos, A. R. Pascoe, and J. Escartín (1997), Corrugated slip surfaces formed at ridge-transform intersections on the Mid-Atlantic Ridge, *Nature*, *385*, 329–332, doi:10.1038/385329a0.

Cannat, M. (1993), Emplacement of mantle rocks in the seafloor at mid-ocean ridges, *J. Geophys. Res.*, *98*, 4163–4172, doi:10.1029/92JB02221.

Cannat, M., C. Mével, and D. Stakes (1991), Stretching of deep crust at the slow-spreading Southwest Indian Ridge, *Tectonophysics*, *190*, 73–94, doi:10.1016/0040-1951(91)90355-V.

Cannat, M., D. Sauter, J. Escartín, L. Lavier, and S. Picazo (2009), Oceanic corrugated surfaces and the strength of the axial lithosphere at slow spreading ridges, *Earth Planet. Sci. Lett.*, *288*, 174–183, doi:10.1016/j.epsl.2009.09.020.

Cherkashev, G. A., V. N. Ivanov, L. I. Lazareva, I. I. Rozhdestvenskaya, M. L. Samovarov, I. M. Poroshina, M. B. Sergeev, T. V. Stepanova, and I. G. Dobretsova (2013), Massive sulfide ores of the northern equatorial Mid-Atlantic Ridge: Oceanology, *53*(5), 607–619, doi:10.1134/S0001437013050032.

Dannowski, A., I. Grevemeyer, C. R. Ranero, G. Ceuleneer, M. Maia, J. P. Morgan, and P. Gente (2010), Seismic structure of an oceanic core complex at the Mid-Atlantic Ridge, 22°19′N, *J. Geophys. Res.*, *115*, B07106, doi:10.1029/2009JB006943.

Delaney, J., D. Mogk, and M. Mottl (1987), Quartz-cemented breccias from the Mid-Atlantic Ridge: Samples of a high-salinity hydrothermal upflow zone, *J. Geophys. Res.*, *92*, 9175–9192, doi:10.1029/JB092iB09p09175.

deMartin, B. J., R. A. Sohn, J. P. Canales, and S. E. Humphris (2007), Kinematics and geometry of active detachment faulting beneath the Trans-Atlantic Geotraverse (TAG) hydrothermal field on the Mid-Atlantic Ridge, *Geology*, *35*, 711–714, doi:10.1130/G23718A.1.

Dick, H. J. B., et al. (2000), A long in-situ section of the lower ocean crust: Results of ODP Leg 176 drilling at the Southwest Indian Ridge, *Earth Planet. Sci. Lett.*, *179*, 31–51, doi:10.1016/S0012-821X(00)00102-3.

Dick, H. J. B., M. A. Tivey, and B. E. Tucholke (2008), Plutonic foundation of a slow-spreading ridge segment: Oceanic core complex at Kane Megamullion, 23°30′N, 45°20′W, *Geochem. Geophys. Geosyst.*, *9*, Q05014, doi:10.1029/2007GC001645.

Di Toro, G., D. L. Goldsby, and T. E. Tullis (2004), Friction falls toward zero in quartz rock as slip velocity approaches seismic rates, *Nature*, *427*, 436–439, doi:10.1038/nature02249.

Doblas, M. (1998), Slickenside kinematic indicators, *Tectonophysics*, *295*, 187–197, doi:10.1016/S0040-1951(98)00120-6.

Escartín, J., and J. P. Canales (2010), Detachments in oceanic lithosphere: Deformation, magmatism, fluid flow, and ecosystems, *EOS Trans. AGU*, *92*(4), 31, doi:10.1029/2011EO040003.

Escartín, J., and M. Cannat (1999), Ultramafic exposures and the gravity signature of the lithosphere near the Fifteen-Twenty Fracture Zone (Mid-Atlantic Ridge, 14°-16.5°N), *Earth Planet. Sci. Lett.*, *171*(3), 411–424.

Escartín, J., G. Hirth, and B. Evans (2001), Strength of slightly serpentinized peridotites: Implications for the tectonics of oceanic lithosphere, *Geology*, *29*, 1023–1026, doi:10.1130/0091-7613(2001)029 < 1023:SOSSPI>2.0.CO;2.

Escartín, J., C. Mével, C. J. MacLeod, and A. M. McCaig (2003), Constraints on deformation conditions and the origin of oceanic detachments: The Mid-Atlantic Ridge core complex at 15°45′N, *Geochem. Geophys. Geosyst.*, *4*, 1067, doi:10.1029/2002GC000472.

Escartín, J., D. K. Smith, J. Cann, H. Schouten, C. H. Langmuir, and S. Escrig (2008), Central role of detachment faults in accretion of slow-spreading oceanic lithosphere, *Nature*, *455*, 790–794, doi:10.1038/nature07333.

Escartín, J., et al. (2017), Tectonic structure, evolution, and the nature of oceanic core complexes and their detachment fault zones (13°20′N and 13°30′N, Mid-Atlantic Ridge), *Geochem. Geophys. Geosyst.*, doi:10.1002/2016GC006775, in press.

Fouquet, Y., et al. (2008), Serpentine cruise-ultramafic hosted hydrothermal deposits on the Mid-Atlantic Ridge: First submersible studies on Ashadze 1 and 2, Logatchev 2 and Krasnov vent fields, *InterRidge News*, *17*, 15–19.

Fouquet, Y., et al. (2010), Geodiversity of hydrothermal processes along the Mid-Atlantic Ridge and ultramafic-hosted mineralization: A new type of oceanic Cu-Zn-Co-Au volcanogenic massive sulfide deposit, in *Diversity of Hydrothermal Systems on Slow Spreading Ocean Ridges*, pp. 321–367, AGU, Washington, D. C., doi:10.1029/2088GM000746.

Frost, B., and J. Beard (2007), On silica activity and serpentinization, *J. Petrol.*, *48*, 1351–1368, doi:10.1093/petrology/egm021.

Gillis, K., and G. Thompson (1993), Metabasalts from the Mid-Atlantic Ridge: New insights into the hydrothermal systems in slow-spreading crust, *Contrib. Mineral. Petrol.*, *113*, 502–523, doi:10.1007/BF00698319.

Grevemeyer, I., T. Reston, and S. Moeller (2013), Microseismicity of the Mid-Atlantic Ridge at 7°S–8°15′S and at the Logatchev Massif oceanic core complex at 14°40′N-14°50′N, *Geochem. Geophys. Geosyst.*, *14*, 3532–3554, doi:10.1002/ggge.20197.

Hansen, L. N., M. J. Cheadle, B. E. John, S. M. Swapp, H. J. B. Dick, B. E. Tucholke, and M. A. Tivey (2013), Mylonitic deformation at the Kane oceanic core complex: Implications for the rheological behavior of oceanic detachment faults, *Geochem. Geophys. Geosyst.*, *14*, 3085–3108, doi:10.1002/ggge.20184.

Hayman, N. W., N. R. Grindlay, M. R. Perfit, P. Mann, S. Leroy, and B. Mercier de Lépinay (2011), Oceanic core complex development at the ultraslow spreading Mid-Cayman Spreading Center, *Geochem. Geophys. Geosyst.*, *12*, Q0AG02, doi:10.1029/2010GC003240.

Heft, L. K., K. M. Gillis, M. A. Pollock, J. A. Karson, and E. M. Klein (2008), Role of upwelling hydrothermal fluids in the development of alteration patterns at fast spreading ridges: Evidence from the sheeted dike complex at Pito Deep, *Geochem. Geophys. Geosyst.*, *9*, Q05O07, doi:10.1029/2007GC001926.

Honnorez, J., J. C. Alt, B.-M. Honnorez-Guerstein, C. Laverne, K. Muehlenbachs, J. Ruiz, and E. Saltzman (1983), Stockwork-like sulfide mineralization in young oceanic crust: Deep sea drilling project hole 504B, in *Initial Reports of the Deep Sea Drilling Project*, vol. 83, pp. 263–282, U.S. Gov. Print. Off., Washington, D. C.

Hooft, E. E., R. S. Detrick, D. R. Toomey, J. A. Collins, and J. Lin (2000), Crustal thickness and structure along three contrasting spreading segments of the Mid-Atlantic Ridge, 33.5°-35°N, *J. Geophys. Res.*, *105*, 8205–8226, doi:10.1029/1999JB900442.

Humphris, S., and G. Thompson (1978), Trace element mobility during hydrothermal alteration of oceanic basalts, *Geochem. Cosmochem. Acta*, *42*, 127–136, doi:10.1016/0016-7037(78)90222-3.

Humphris, S., P. Herzig, and D. Miller (1996), Introduction and principal results, in *Proceeding of the Ocean Drilling Program Initial Reports*, vol. 158, pp. 5–14, U.S. Ocean Drill. Program, College Station, Tex., doi:10.2973/odp.proc.ir.158.101.1996.

Ishizuka, H. (1999), Pumpellyite from the oceanic crust, DSDP/ODP Hole 504B, *Mineral. Mag.*, *63*, 891–900.
Karson, J. A., G. L. Früh-Green, D. S. Kelley, E. A. Williams, D. R. Yoerger, and M. Jakuba (2006), Detachment shear zone of the Atlantis Massif core complex, Mid-Atlantic Ridge, 30°N, *Geochem. Geophys. Geosyst.*, *7*, Q06016, doi:10.1029/2005GC001109.
Kohlstedt, D. L., B. Evans, and S. J. Mackwell (1995), Strength of the lithosphere: Constraints imposed by laboratory experiments, *J. Geophys. Res.*, *100*, 17,587–17,602.
Kong, L., S. Solomon, and G. Purdy (1992), Microearthquake characteristics of a mid-ocean ridge along-axis high, *J. Geophys. Res.*, *97*, 1659–1685, doi:10.1029/91JB02566/epdf.
Laverne, C., D. Vanko, P. Tartarotti, and J. C. Alt (1995), Chemistry and geothermometry of secondary minerals from the deep sheeted dyke complex, hole 504B, in *Proceedings of Ocean Drilling Project Scientific Results*, vol. 137/140, edited by J. Erzinger et al., pp. 167–188, Ocean Drill. Program, College Station, Tex.
MacLeod, C. J., et al. (2002), Direct geological evidence for oceanic detachment faulting: The Mid-Atlantic Ridge, 15°45′N, *Geology*, *30*, 879–882, doi:10.1130/0091-7613-31.1.e15.
MacLeod, C. J., R. C. Searle, B. J. Murton, J. F. Casey, C. Mallows, S. C. Unsworth, K. L. Achenbach, and M. Harris (2009), Life cycle of oceanic core complexes, *Earth Planet. Sci. Lett.*, *287*, 333–344, doi:10.1016/j.epsl.2009.08.016.
Mallows, C., and R. C. Searle (2012), A geophysical study of oceanic core complexes and surrounding terrain, mid-Atlantic ridge 10°N-14°N, *Geochem. Geophys. Geosyst.*, *13*, Q0AG08, doi:10.1029/2012GC004075.
McCaig, A. M., R. A. Cliff, J. Escartín, A. E. Fallick, and C. J. MacLeod (2007), Oceanic detachment faults focus very large volumes of black smoker fluids, *Geology*, *35*, 935–938, doi:10.1130/G23657A.1.
McCaig, A. M., A. Delacour, A. E. Fallick, T. Castelain, and G. L. Früh-Green (2010), Detachment fault control on hydrothermal circulation systems: Interpreting the subsurface beneath the TAG hydrothermal field using the isotopic and geological evolution of oceanic core complexes in the Atlantic, in *Diversity of Hydrothermal Systems on Slow Spreading Ocean Ridges, Geophys. Monogr. Ser.*, edited by P. A. Rona et al., vol. 188, pp. 207–239, doi:10.1029/2008GM000729.
Mével, C. (1981), Occurrence of pumpellyite in hydrothermally altered basalts from the Vema fracture zone (Mid-Atlantic Ridge), *Contrib. Mineral. Petrol.*, *76*, 386–393, doi:10.1007/BF00371480.
Miranda, E. A., and B. E. John (2010), Strain localization along the Atlantis Bank oceanic detachment fault system, Southwest Indian Ridge, *Geochem. Geophys. Geosyst.*, *11*, Q04002, doi:10.1029/2009GC002646.
Morris, A., J. S. Gee, N. Pressling, B. E. John, C. J. MacLeod, C. B. Grimes, and R. C. Searle (2009), Footwall rotation in an oceanic core complex quantified using reoriented Integrated Ocean Drilling Program core samples, *Earth Planet. Sci. Lett.*, *287*, 217–228, doi:10.1016/j.epsl.2009.08.007.
Mottl, M. (1983), Metabasalts, axial hot springs, and the structure of hydrothermal systems at mid-ocean ridges, *Geol. Soc. Am. Bull.*, *94*, 161–180, doi:10.1130/0016-7606(1983)94 < 161:MAHSAT>2.0.CO;2.
Nicosevici, T., and R. Garcia (2013), *Efficient 3D Scene Modeling and Mosaicing*, Springer, Berlin Heidelberg.
Noda, H., K. Kanagawa, T. Hirose, and A. Inoue (2011), Frictional experiments of dolerite at intermediate slip rates with controlled temperature: Rate weakening or temperature weakening?, *J. Geophys. Res.*, *116*, B07306, doi:10.1029/2010JB007945.
O'Hanley, D. S. (1996), *Serpentinites: Records of Tectonic and Petrological History*, 277 pp., Oxford Univ. Press.
Olive, J.-A., M. D. Behn, and B. E. Tucholke (2010), The structure of oceanic core complexes controlled by the depth distribution of magma emplacement, *Nat. Geosci.*, *3*, 491–495, doi:10.1038/ngeo888.
Picazo, S., M. Cannat, A. Delacour, J. Escartín, S. Rouméjon, and S. Silantyev (2012), Deformation associated with the denudation of mantle-derived rocks at the Mid-Atlantic Ridge 13°-15°N: The role of magmatic injections and hydrothermal alteration, *Geochem. Geophys. Geosyst.*, *13*, Q04G09, doi:10.1029/2012GC004121.
Reston, T. J., W. Weinrebe, I. Grevemeyer, E. R. Flueh, N. C. Mitchell, L. Kirstein, C. Kopp, and H. Kopp (2002), A rifted inside corner massif on the Mid-Atlantic Ridge at 5°S, *Earth Planet. Sci. Lett.*, *200*, 255–269, doi:10.1016/S0012-821X(02)00636-2.
Reston, T. J., M. Falder, C. Peirce, N. Simao, R. Searle, and C. J. MacLeod (2016), The role of detachment faulting in slow spreading: First results from cruise JC132 to the MAR at 13°N, Abstract A14B-1234 presented at AGU Fall Meeting, AGU, San Francisco, Calif., 12–16 Dec.
Schouten, H., D. K. Smith, J. R. Cann, and J. Escartín (2010), Tectonic versus magmatic extension in the presence of core complexes at slow-spreading ridges from a visualization of faulted seafloor topography, *Geology*, *38*, 615–618, doi:10.1130/G30803.1.
Schroeder, T., and B. E. John (2004), Strain localization on an oceanic detachment fault system, Atlantis Massif, 30°N, Mid-Atlantic Ridge, *Geochem. Geophys. Geosyst.*, *5*, Q11007, doi:10.1029/2004GC000728.
Schroeder, T., M. J. Cheadle, H. J. B. Dick, U. Faul, J. F. Casey, and P. B. Kelemen (2007), Nonvolcanic seafloor spreading and corner-flow rotation accommodated by extensional faulting at 15°N on the Mid-Atlantic Ridge: A structural synthesis of ODP Leg 209, *Geochem. Geophys. Geosyst.*, *8*, Q06015, doi:10.1029/2006GC001567.
Searle, R. C., M. Cannat, K. Fujioka, C. Mével, H. Fujimoto, A. Bralee, and L. Parson (2003), FUJI dome: A large detachment fault near 64°E on the very slow-spreading southwest Indian Ridge, *Geochem. Geophys. Geosyst.*, *4*(8), 9105, doi:10.1029/2003GC000519.
Simao, N., J. Escartín, J. Goslin, J. Haxel, M. Cannat, and R. Dziak (2010), Regional seismicity of the Mid-Atlantic Ridge: Observations from autonomous hydrophone arrays, *Geophys. J. Int.*, *183*, 1559–1578, doi:10.1111/j.1365-246X.2010.04815.x.
Smith, D. K., J. R. Cann, and J. Escartín (2006), Widespread active detachment faulting and core complex formation near 13°N on the Mid-Atlantic Ridge, *Nature*, *442*, 440–443, doi:10.1038/nature04950.
Smith, D. K., J. Escartín, H. Schouten, and J. R. Cann (2008), Fault rotation and core complex formation: Significant processes at slow-spreading mid-ocean ridges (Mid-Atlantic Ridge, 13°–15°N), *Geochem. Geophys. Geosyst.*, *9*, Q03003, doi:10.1029/2007GC001699.
Toomey, D., S. Solomon, G. Purdy, and M. Murray (1985), Microearthquakes beneath the median valley of the Mid-Atlantic Ridge near 23°N: Hypocenters and focal mechanisms, *J. Geophys. Res.*, *90*, 5443–5458, doi:10.1029/JB090iB07p05443.
Tucholke, B. E., J. Lin, and M. C. Kleinrock (1998), Megamullions and mullion structure defining oceanic metamorphic core complexes on the Mid-Atlantic Ridge, *J. Geophys. Res.*, *103*, 9857–9866, doi:10.1029/98JB00167.
Tucholke, B. E., M. D. Behn, W. R. Buck, and J. Lin (2008), Role of melt supply in oceanic detachment faulting and formation of megamullions, *Geology*, *36*, 455–458, doi:10.1130/G24639A.1.
Wilson, D. S., et al. (2006), Drilling into gabbros in intact oceanic crust, *Science*, *312*, 1016–1020, doi:10.1126/science.1126090.

Geochemistry, Geophysics, Geosystems

Supporting Information for

Pervasive silicification and hangingwall overplating along the 13°20'N oceanic detachment fault (Mid-Atlantic Ridge)

D. Bonnemains[1], J. Escartín[1], C. Mével[1], M. Andreani[2], A. Verlaguet[3]

[1]Institut de Physique du Globe de Paris, CNRS UMR 7154, Paris, France
[2]Laboratoire de Géologie de Lyon, UMR 5672, ENS, Université Lyon 1, Lyon, France
[3]Institut des Sciences de la Terre de Paris, CNRS, Sorbonne Universités, Université Paris 6, Paris, France

Contents of this file

Introduction

This supporting information provides data relative to chemical analyses (Table S1) and additional figures of in-situ fault rocks collected on the 13°20'N detachment fault zone (Figure S1 to S11).

Table S1: Electron microprobe analyses of amphibole.

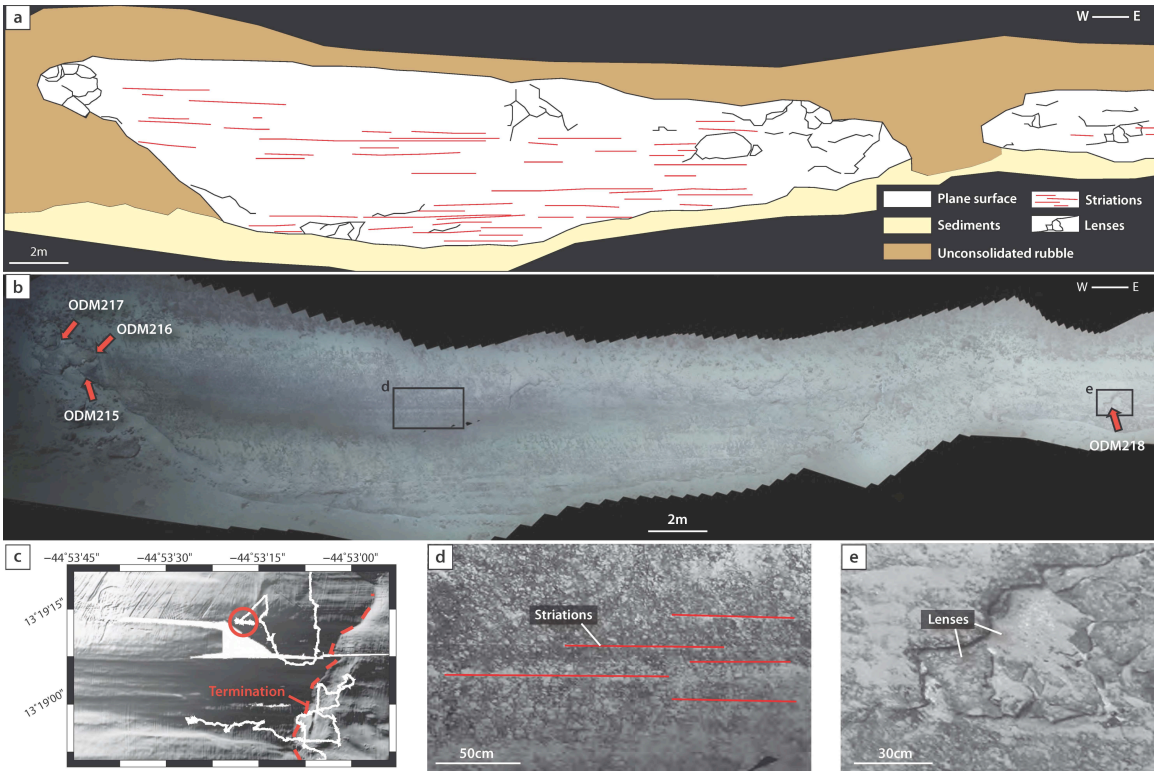

Figure S1: (a) Geological interpretation of (b) videomosaic ROV high-resolution video survey of outcrop #2 (see location in **Figure 1b**). Sampling positions are indicated on (b) by red arrows and the sample name. (c) Shaded microbathymetry of outcrop #2. The outcrop location is indicated with a red circle, the corrugated surface termination is shown with a dotted red line, and the ROV paths with white lines. (d) E-W striations (red lines) are widespread throughout the fault outcrop surface. (e) Fault plane surfaces are made of plane scales or lenses from several centimeters to a meter wide.

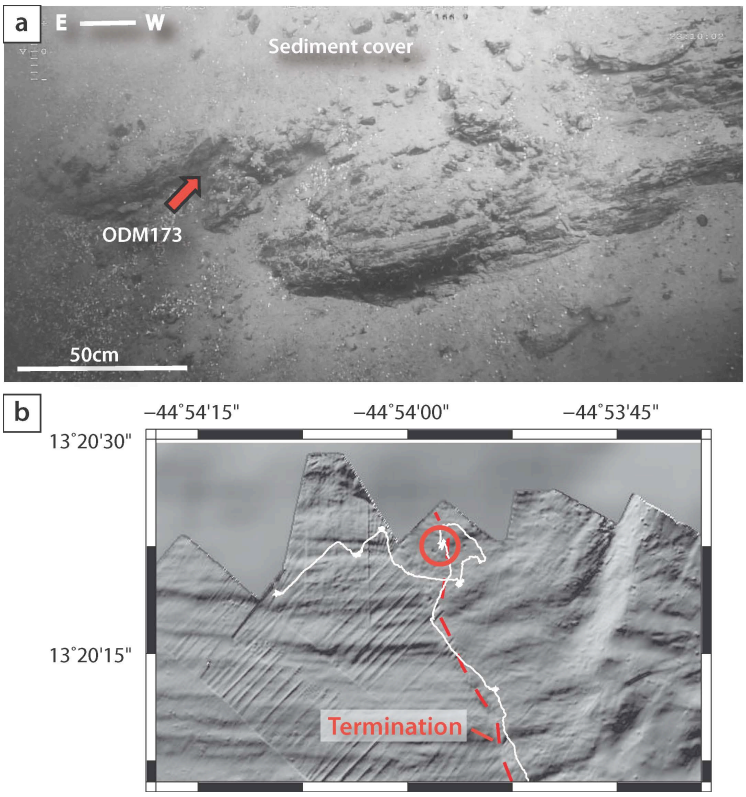

Figure S2: (a) Photograph of outcrop #3 (see location in **Figure 1b**) and location of ODM173 indicated by a red arrow. (b) Shaded relief microbathymetry of outcrop #3 area. The outcrop location is indicated with a red circle, the corrugated surface termination is shown with a dotted red line, and the ROV paths with white lines.

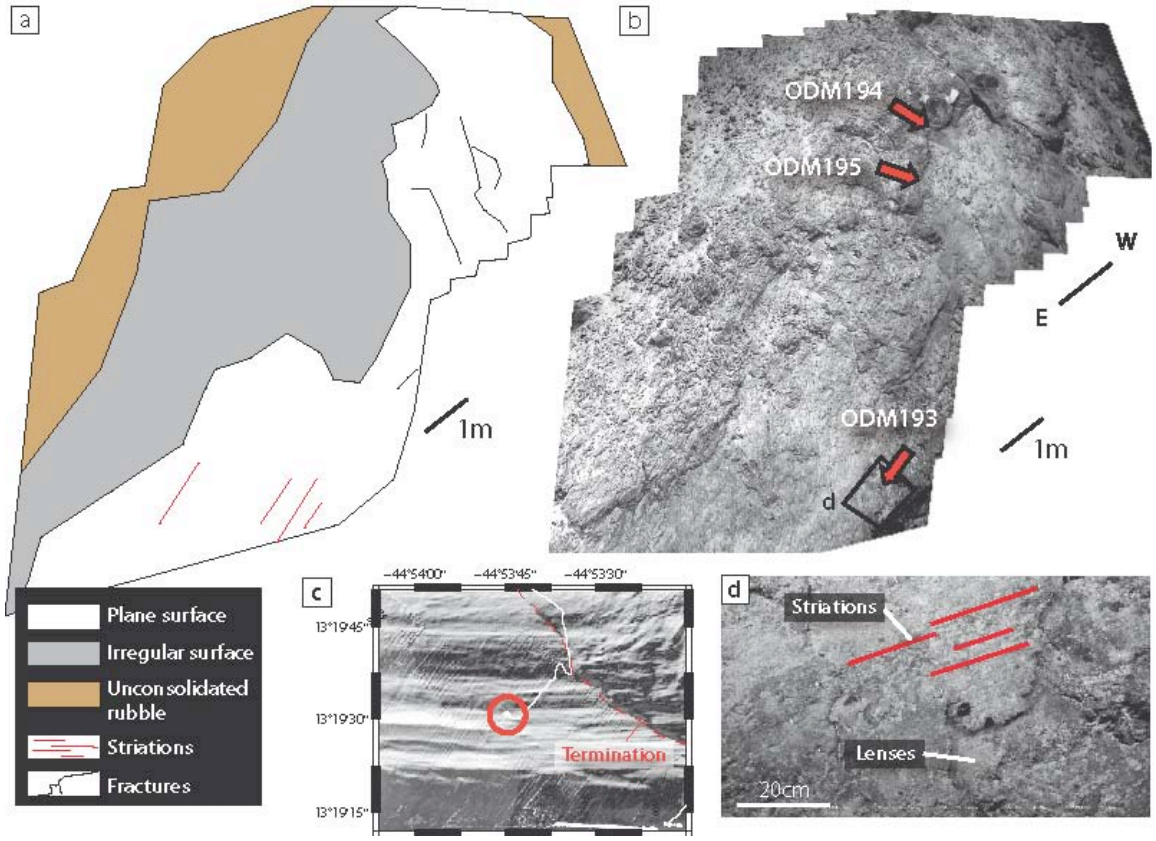

Figure S3: (a) Geological interpretation of (b) videomosaic ROV high-resolution video survey of outcrop #4 (see location in **Figure 1b**). Sampling positions are indicated on (b) by red arrows and the sample name. (c) Shaded relief microbathymetry of outcrop #4. The outcrop location is indicated with a red circle, the corrugated surface termination is shown with a dotted red line, and the ROV paths with white lines. (d) E-W striations (red lines) are widespread on the whole outcrop surface. Plane surfaces are made of plane scales or lenses from several centimeters to a meter wide.

Figure S4: (a) Geological interpretation of (b) videomosaic ROV high-resolution video survey of outcrop #5 (see location in **Figure 1b**). ODM128 position is indicated on (b) by a red arrow. (c) Shaded relief microbathymetry of outcrop #2. The outcrop location is indicated with a red circle, the corrugated surface termination is shown with a dotted red line, and the ROV paths with white lines.

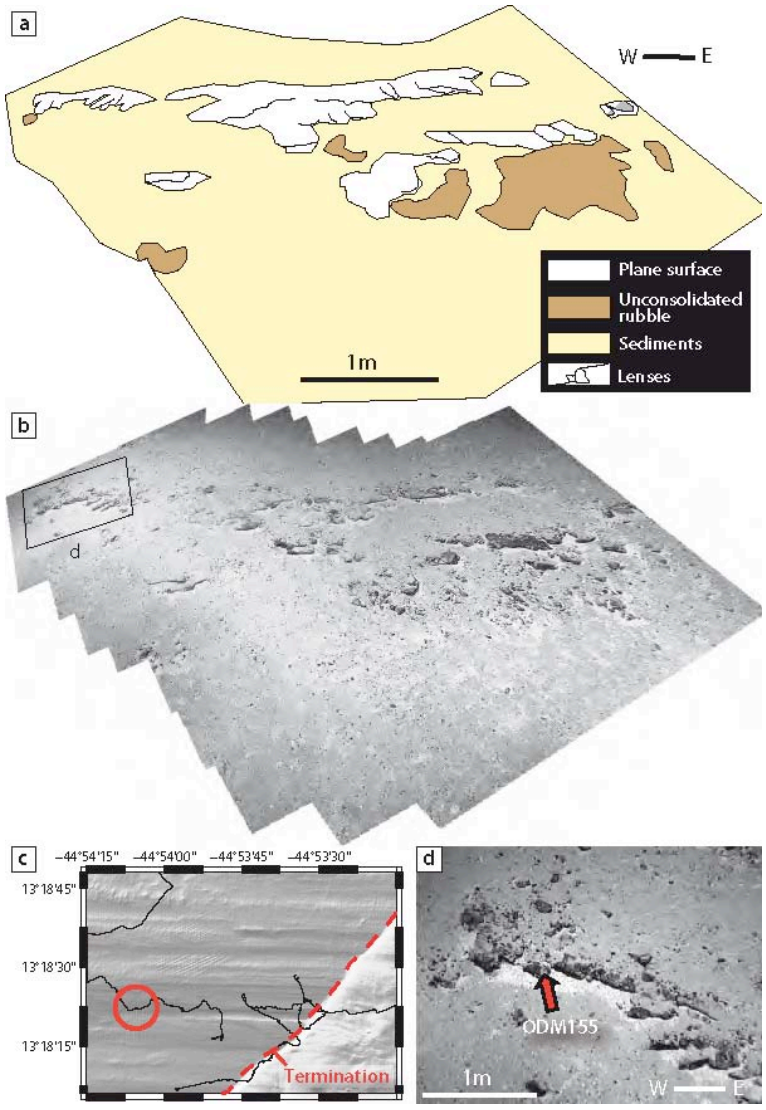

Figure S5: (a) Geological interpretation of (b) videomosaic ROV high-resolution video survey of outcrop #6 (see location in **Figure 1b**). (c) Shaded relief microbathymetry of outcrop #2. The outcrop location is indicated with a red circle, the corrugated surface termination is shown with a dotted red line, and the ROV paths with white lines. (d) Close up on the location of ODM155 (red arrow).

Figure S6: (a) Macro-photograph of the schistosed mafic fault rock ODM128, located along outcrop #5 (see **Figure 1b** for location). (b) View of a reflective and striated surface. (c) Schistosity is parallel to the surface and is formed by alignments of chlorite-filled veins. (d) Microlithons are either matrix of fragments of clasts.

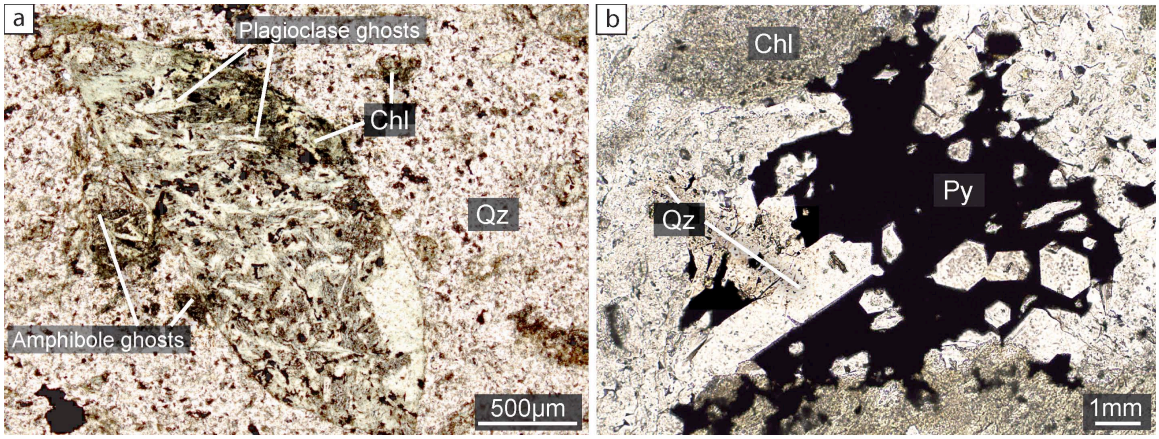

Figure S7: Microphotographs of highly silicified sample ODM218 under parallel nicols of: (a) a chloritized clast where ghosts of primary minerals can be recognized by their texture and similarity with clasts from moderately silicified samples (**Figure 7a**); (b) Intergrowth of pyrite and quartz.

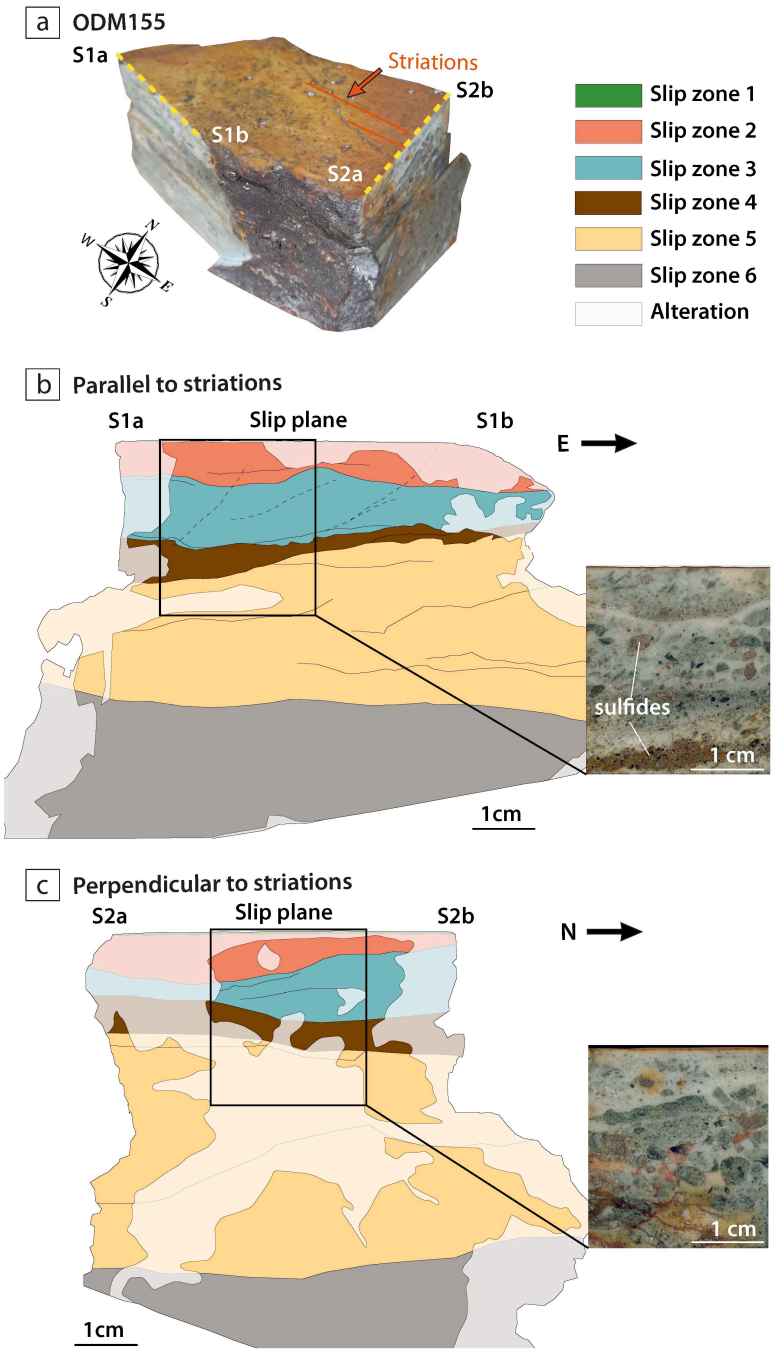

Figure S8: (a) Location of the two sections of the oriented ODM155 fault rock: one parallel (b) and the other perpendicular (c) to striation direction. (b-c) Interpretation of cut surfaces whose structures are shown in the insets. Different slip zones are distinguished by their color and clast content. Internal structures are indicated by black lines, and alteration zones and halo by the whiter zones, primarily along the borders of the sample.

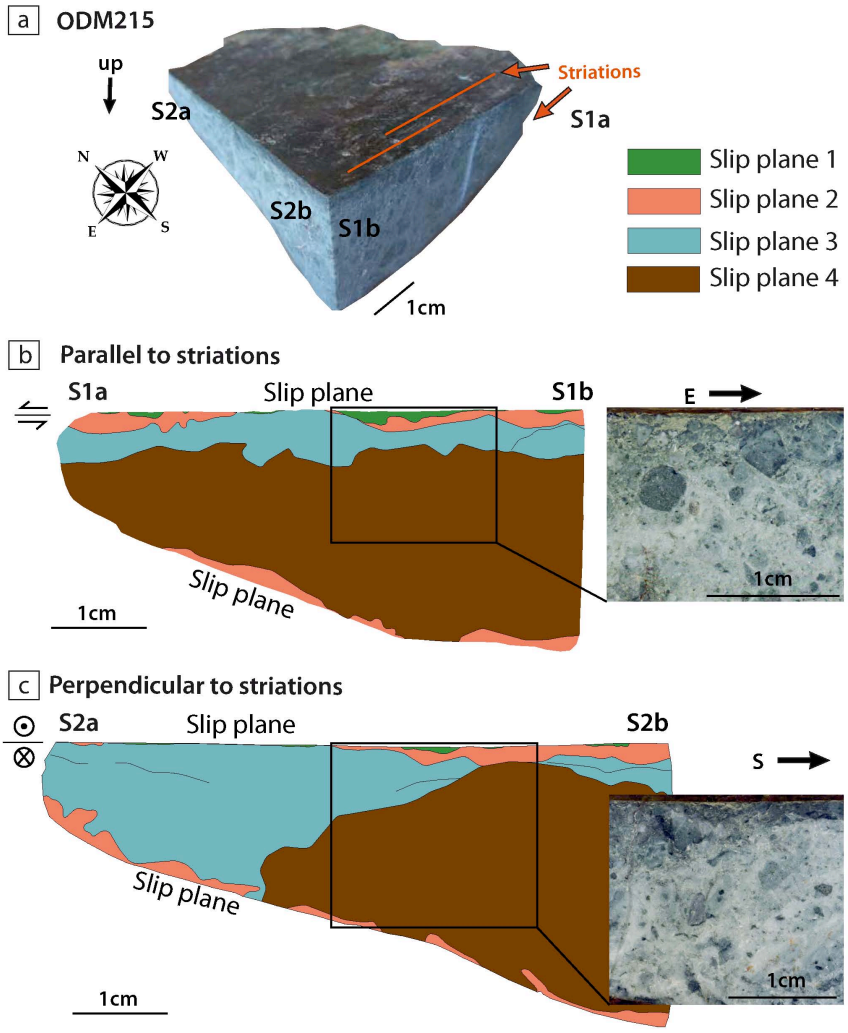

Figure S9: (a) Location of the two sections of the oriented ODM215 fault rock: one parallel (b) and the other perpendicular (c) to striation direction. (b-c) Interpretation of cut surfaces whose structures are shown in the insets. Different slip zones are distinguished by their color and differences in clast content and size. Internal structures are indicated by black lines.

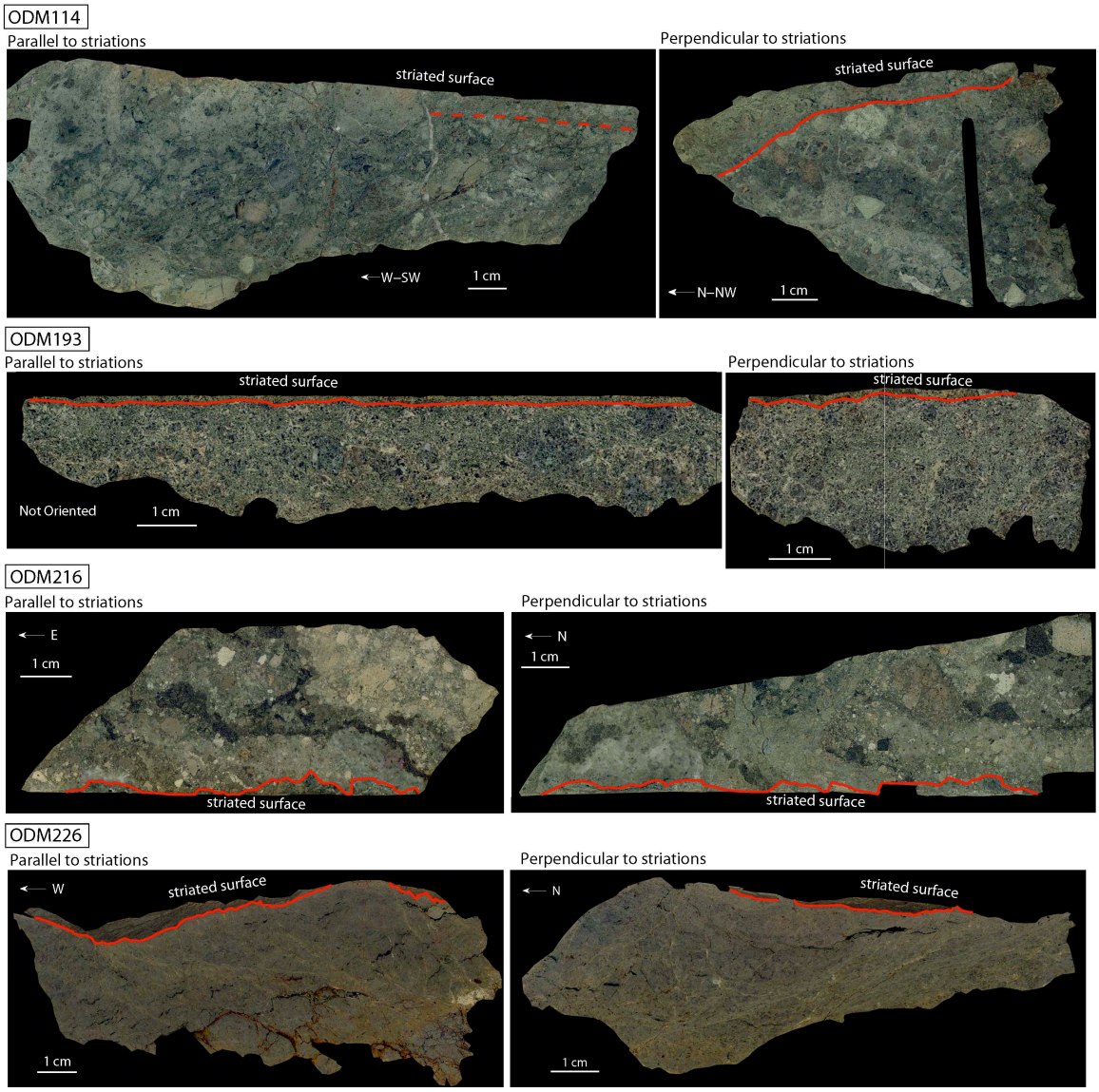

Figure S10: Parallel- and perpendicular-to-striations sections for samples containing two slip zone (red lines) below their striated surfaces.

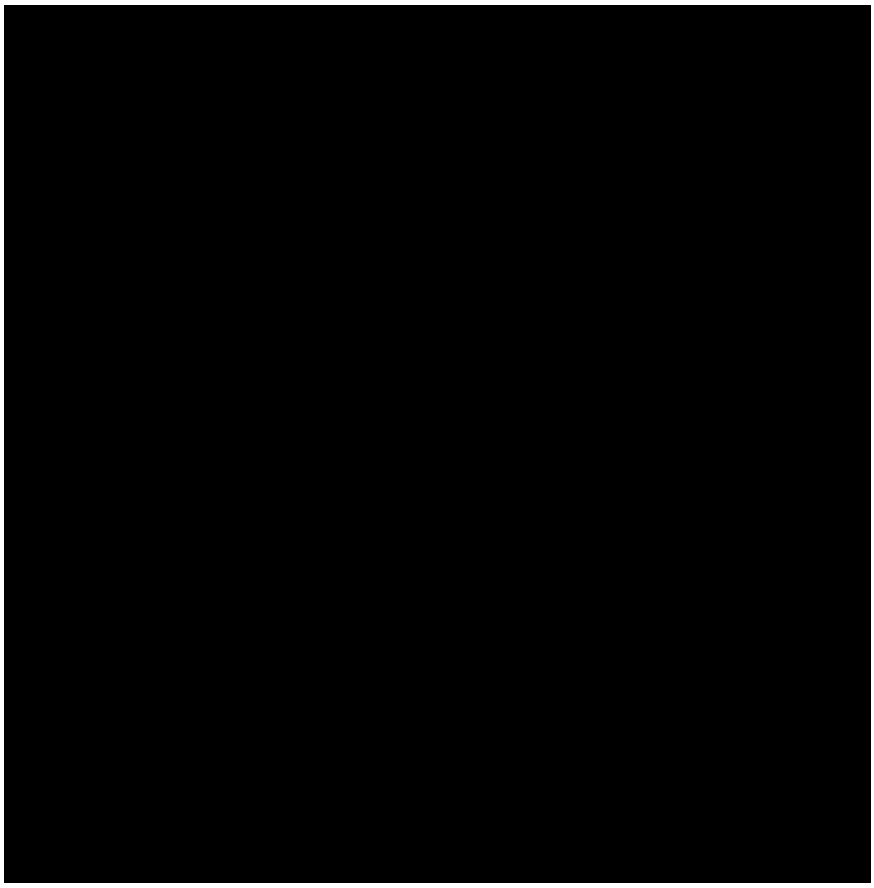

Figure S11: Macro-photographs of two representative samples collected on the corrugated detachment fault surface. Both under greenschist facies, (b) shows similar microstructures than with situ samples (matrix-supported breccia, sulfides), suggesting that its deformation was fault related, and (c) display of recognizable fragments of now altered glass, indicating a hyaloclastic origin.

Sample	ODM193													ODM194					
Oxide wt.%																			
SiO_2	53.90	52.14	51.90	52.64	52.37	52.60	44.91	46.53	48.96	53.64	52.41	54.25	53.31	50.54	49.23	51.88	49.08	49.54	50.65
TiO_2	0.46	0.51	0.29	0.50	0.39	0.50	0.99	0.98	0.83	0.39	0.66	0.61	0.51	0.60	0.90	0.49	0.84	0.70	0.53
Al_2O_3	3.06	4.15	4.40	3.98	3.53	3.45	11.09	9.70	8.48	3.15	4.64	2.63	3.28	6.65	7.70	5.29	7.29	6.71	5.36
Cr_2O_3	0.05	0.10	0.00	0.03	0.03	0.00	0.16	0.04	0.31	0.03	0.00	0.03	0.04	0.61	0.68	0.96	0.09	0.73	0.49
FeO	10.95	13.78	12.33	11.13	14.49	14.62	12.60	12.17	9.28	10.28	10.91	11.71	11.88	9.69	9.48	8.79	10.95	10.00	10.32
MnO	0.24	0.26	0.13	0.08	0.02	0.07	0.10	0.11	0.06	0.23	0.09	0.35	0.12	0.06	0.11	0.17	0.10	0.08	0.13
MgO	16.68	13.68	15.09	16.72	13.87	14.14	13.94	14.43	16.52	17.35	16.89	16.81	16.85	16.40	16.13	16.49	15.95	16.18	16.78
NiO	0.12	0.07	0.11	0.18	0.00	0.00	0.00	0.00	0.00	0.00	0.17	0.00	0.06	0.23	0.00	0.04	0.00	0.05	0.00
CaO	11.89	12.17	12.42	11.67	12.12	12.04	12.09	11.83	12.32	11.72	11.00	12.20	11.45	11.58	11.49	12.09	11.78	11.77	11.66
Na_2O	0.49	0.62	0.59	0.78	0.53	0.48	2.33	1.91	1.69	0.60	0.85	0.45	0.65	1.36	1.52	0.98	1.43	1.35	1.20
K_2O	0.03	0.01	0.05	0.03	0.04	0.04	0.17	0.16	0.04	0.04	0.04	0.03	0.04	0.22	0.17	0.19	0.25	0.24	0.22
Cl	0.04	0.01	0.01	0.07	0.01	0.03	0.10	0.12	0.07	0.06	0.06	0.07	0.08	0.10	0.08	0.11	0.12	0.13	0.14
Total	97.90	97.51	97.34	97.80	97.39	97.88	98.39	97.96	98.50	97.47	97.70	99.13	98.25	98.04	97.45	97.47	97.85	97.48	97.47
Structural formula (*a.p.f.u.*)																			
Si	7.68	7.57	7.51	7.53	7.63	7.62	6.54	6.77	6.96	7.65	7.48	7.66	7.60	7.21	7.07	7.41	7.07	7.14	7.29
Ti	0.05	0.06	0.03	0.05	0.04	0.05	0.11	0.11	0.09	0.04	0.07	0.07	0.05	0.06	0.10	0.05	0.09	0.08	0.06
Al	0.51	0.71	0.75	0.67	0.61	0.59	1.90	1.66	1.42	0.53	0.78	0.44	0.55	1.12	1.30	0.89	1.24	1.14	0.91
Cr	0.01	0.01	0.00	0.00	0.00	0.00	0.02	0.00	0.03	0.00	0.00	0.00	0.00	0.07	0.08	0.11	0.01	0.08	0.06
Fe^{+2}	1.30	1.67	1.49	1.33	1.76	1.77	1.54	1.48	1.10	1.23	1.30	1.38	1.42	1.16	1.14	1.05	1.32	1.21	1.24
Mn	0.03	0.03	0.02	0.01	0.00	0.01	0.01	0.01	0.01	0.03	0.01	0.04	0.01	0.01	0.01	0.02	0.01	0.01	0.02
Mg	3.54	2.96	3.26	3.56	3.01	3.05	3.03	3.13	3.50	3.69	3.59	3.54	3.58	3.49	3.45	3.51	3.43	3.48	3.60
Ni	0.01	0.01	0.01	0.02	0.00	0.00	0.00	0.00	0.00	0.00	0.02	0.00	0.01	0.03	0.00	0.00	0.00	0.01	0.00
Ca	1.81	1.89	1.93	1.79	1.89	1.87	1.89	1.84	1.88	1.79	1.68	1.85	1.75	1.77	1.77	1.85	1.82	1.82	1.80
Na	0.14	0.18	0.17	0.22	0.15	0.14	0.66	0.54	0.47	0.17	0.24	0.12	0.18	0.38	0.42	0.27	0.40	0.38	0.34
K	0.01	0.00	0.01	0.00	0.01	0.01	0.03	0.03	0.01	0.01	0.01	0.00	0.01	0.04	0.03	0.03	0.05	0.04	0.04
Tot	15.09	15.10	15.17	15.19	15.11	15.11	15.73	15.58	15.46	15.13	15.18	15.11	15.16	15.34	15.37	15.19	15.44	15.38	15.35

Sample	ODM194					ODM195										ODM224				
Oxide wt.%																				
SiO_2	54.25	52.12	50.94	52.06	52.42	53.04	53.51	53.47	52.47	50.00	54.26	51.79	52.24	50.97	49.89	48.86	49.50	48.17	48.65	52.80
TiO_2	0.40	0.97	0.50	0.33	0.30	0.16	0.14	0.41	0.36	0.17	0.52	0.35	0.26	0.54	0.22	0.35	0.81	1.61	0.11	0.25
Al_2O_3	2.88	4.16	5.43	4.00	3.19	3.21	3.00	2.04	3.80	3.14	1.73	4.11	1.38	5.15	7.56	3.95	3.99	5.73	7.10	4.81
Cr_2O_3	0.00	0.00	1.43	0.45	0.08	0.02	0.00	0.00	0.00	0.04	0.03	0.32	0.00	0.27	0.00	0.03	0.04	0.06	0.10	0.04
FeO	10.41	11.51	9.56	12.32	13.99	12.61	11.39	12.74	11.35	19.32	13.43	13.46	19.09	12.01	10.96	17.80	18.16	15.25	12.10	9.27
MnO	0.08	0.26	0.21	0.07	0.06	0.21	0.11	0.29	0.21	0.33	0.24	0.22	0.32	0.26	0.26	0.37	0.36	0.51	0.31	0.33
MgO	18.18	16.61	15.71	14.80	14.71	15.32	15.94	15.66	15.87	12.03	15.82	14.83	11.76	15.03	16.17	13.48	12.75	12.99	17.98	17.60
NiO	0.15	0.00	0.18	0.03	0.02	0.08	0.04	0.00	0.07	0.00	0.14	0.08	0.00	0.05	0.07	0.06	0.02	0.00	0.00	0.00
CaO	11.15	11.79	12.01	12.03	11.56	12.35	12.34	11.80	11.87	9.14	11.34	11.27	12.14	12.14	11.88	10.99	10.04	10.76	9.20	12.02
Na_2O	0.52	0.76	0.85	0.63	0.46	0.48	0.33	0.22	0.50	0.44	0.24	0.69	0.15	0.68	1.25	0.48	0.81	0.76	0.27	0.60
K_2O	0.08	0.15	0.11	0.11	0.06	0.03	0.00	0.02	0.01	0.03	0.04	0.04	0.00	0.07	0.02	0.04	0.12	0.09	0.04	0.04
Cl	0.13	0.13	0.05	0.03	0.05	0.01	0.00	0.00	0.00	0.29	0.02	0.07	0.04	0.00	0.01	0.08	0.19	0.01	0.01	0.00
Total	98.24	98.22	96.99	96.86	96.89	97.58	96.75	96.59	96.51	94.90	97.86	97.24	97.31	97.21	98.29	96.48	96.80	95.94	95.85	97.73
Structural formula (*a.p.f.u.*)																				
Si	7.67	7.44	7.35	7.57	7.65	7.65	7.72	7.77	7.60	7.64	7.80	7.53	7.79	7.39	7.13	7.35	7.42	7.20	7.11	7.48
Ti	0.04	0.10	0.05	0.04	0.03	0.02	0.02	0.04	0.04	0.02	0.06	0.04	0.03	0.06	0.02	0.04	0.09	0.18	0.01	0.03
Al	0.48	0.70	0.92	0.69	0.55	0.55	0.51	0.35	0.65	0.57	0.29	0.70	0.24	0.88	1.27	0.70	0.71	1.01	1.22	0.80
Cr	0.00	0.00	0.16	0.05	0.01	0.00	0.00	0.00	0.00	0.00	0.00	0.04	0.00	0.03	0.00	0.00	0.01	0.01	0.01	0.00
Fe^{+2}	1.23	1.37	1.15	1.50	1.71	1.52	1.37	1.55	1.37	2.47	1.62	1.64	2.38	1.46	1.31	2.24	2.28	1.91	1.48	1.10
Mn	0.01	0.03	0.03	0.01	0.01	0.03	0.01	0.04	0.03	0.04	0.03	0.03	0.04	0.03	0.03	0.05	0.05	0.07	0.04	0.04
Mg	3.83	3.53	3.38	3.21	3.20	3.30	3.43	3.39	3.43	2.74	3.39	3.22	2.61	3.25	3.44	3.02	2.85	2.90	3.92	3.72
Ni	0.02	0.00	0.02	0.00	0.00	0.01	0.00	0.00	0.01	0.00	0.02	0.01	0.00	0.01	0.01	0.01	0.00	0.00	0.00	0.00
Ca	1.69	1.80	1.86	1.87	1.81	1.91	1.91	1.84	1.84	1.50	1.75	1.76	1.94	1.89	1.82	1.77	1.61	1.72	1.44	1.82
Na	0.14	0.21	0.24	0.18	0.13	0.14	0.09	0.06	0.14	0.13	0.07	0.20	0.04	0.19	0.35	0.14	0.24	0.22	0.08	0.17
K	0.01	0.03	0.02	0.02	0.01	0.01	0.00	0.00	0.00	0.00	0.01	0.01	0.00	0.01	0.00	0.01	0.02	0.02	0.01	0.01
Tot	15.13	15.23	15.18	15.13	15.11	15.12	15.06	15.04	15.11	15.12	15.03	15.16	15.08	15.20	15.39	15.33	15.26	15.23	15.31	15.17